**AN ABSTRACT OF THE THESIS OF**

Matthew R. Mueller for the degree of Master of Science in Electrical and Computer Engineering presented on September 8, 1994. Title: Development and Characterization of AlInN as an Alternating-Current Thin-Film Electroluminescent Display Phosphor.

Redacted for Privacy

Abstract approved: _____
Dr. John F. Wager

The goal of this thesis is to evaluate AlInN as an alternating-current thin-film electroluminescent (ACTFEL) display phosphor. ACTFEL devices are fabricated using RF sputtering for the phosphor deposition. $Al_{0.8}In_{0.2}$:$Eu_2O_3$ and $Al_{0.9}In_{0.1}$:$EuF_3$ targets are used with nitrogen diluted with argon to reactively sputter AlInON thin-films. All of the thin-films deposited to date possess a large amount of oxygen which is either unintentionally incorporated or is intentionally incorporated via the use of nitrous oxide as a process gas. Most of the phosphors are deposited at room temperature, although a few are deposited at an elevated temperature of approximately 200 C. Some phosphors and ACTFEL devices are subjected to post-deposition rapid thermal annealing. Photoluminescence from the deposited AlInON thin-film is a dim red after annealing at 500 C or above. Charge transport is observed in AlInON ACTFEL devices and dim white light is produced, which is attributed to hot electron luminescence. A maximum brightness of 0.009 fL is measured for the AlInON ACTFEL devices fabricated to date. No crystallinity is observed in the AlInON thin-films after annealing at temperatures of 650 C or for films deposited at 200 C. Future work on the development of AlInON as an ACTFEL phosphor should focus on the elimination of oxygen in the deposited film by replacement of the process gas manifold and on strategies to increase the substrate

temperature during deposition so that AlInN thin-films with better crystallinity may be obtained.

# Development and Characterization of AlInN as an Alternating-Current Thin-Film Electroluminescent Display Phosphor

by

Matthew R. Mueller

A THESIS

submitted to

Oregon State University

in partial fulfillment of
the requirements for the
degree of

Master of Science

Completed September 8, 1994

Commencement June 1995

**APPROVED:**

Redacted for Privacy

Professor of Electrical and Computer Engineering in charge of major

Redacted for Privacy

Head of Department of Electrical and Computer Engineering

Redacted for Privacy

Dean of Graduate School

Date thesis is presented: September 8, 1994

Typed by researcher for: Matthew R. Mueller

## ACKNOWLEDGEMENTS

I wish to thank Dr. John F. Wager for his patience, guidance, and support throughout my program. Without his assistance this work would not have been possible. I also wish to thank Dr. Tom Plant, Dr. Ben Lee, and Dr. Mike Quinn for serving on my committee.

I wish to thank a number of people who supported this research. Manfred Dittrich, Art Neeley, and Leon Ungier provided valuable technical assistance at several points in the project. Ming Ang, Long Pham, Robert Thuemler, and Tin Nguyen did their best to educate me in the ways of ACTFEL device processing, physics, and document preparation.

I wish to thank Planar Systems Inc. for providing the substrates used in this research, and Sey-Shing Sun and Bob Zimmerman for their technical assistance.

I wish to thank my family for their support throughout this project.

Finally, I wish to thank William Manchester, Barbara H. Tuchman, Jim Thompson, Tony Hillerman, and Elmore Leonard for entertaining me when science failed to.

This work was supported in part by the U.S. Army Research Office under contract no. DAAL03-91-G-0242 and DAAH04-94-G-0183.

## TABLE OF CONTENTS

## LIST OF FIGURES

## LIST OF TABLES

Development and Characterization of AlInN as an Alternating-Current Thin-Film Electroluminescent Display Phosphor

# CHAPTER 1 - INTRODUCTION

Information display has been dominated by cathode ray tubes. However, many emerging technologies are stimulating the development of new types of displays that better suit their applications. Portable, compact displays for personal computers, automobiles, and military vehicles are one such niche. Another niche is small displays which can be mounted in goggles for use in virtual reality simulations or military applications. These displays must be scalable to the required size, lightweight, and bright.

Flat panel displays (FPDs) possess these qualities. There are several different types of FPDs currently available, including liquid crystal displays (LCDs), plasma displays, and electroluminescent (EL) devices. LCDs dominate the FPD market presently, but EL devices have been gaining ground since 1974 when Inoguchi *et al.* [1] demonstrated high luminance and stable performance from alternating-current thin-film electroluminescent (ACTFEL) devices. ACTFEL devices have some advantages over LCDs. These advantages include being more rugged (due to their solid-state construction), having a wider viewing angle, and being emissive in nature and therefore not requiring additional backlighting. Much research has been undertaken to develop practical EL displays for both monochrome and full-color applications.

The dominant phosphor material used today in EL devices is zinc sulfide. Doping ZnS with manganese (ZnS:Mn) produces a bright yellow light which is used in monochromatic displays. Full-color displays require red, blue, and green light (the primary colors). Green light can be produced by doping ZnS with terbium [2,3] while red light can be obtained by using ZnS:Mn with a red filter of CdSSe [4]. Bright blue light remains a problem to be solved.

Other alternative material systems for providing red and blue light are being evaluated. Oxides and nitrides can form phosphors [5,6,7] with advantages as well as disadvantages over ZnS material systems. The advantages of the alternative phosphors are their improved chemical stability and their ease of deposition. The primary disadvantage is the lower brightness currently demonstrated. It is believed that the poor brightness of the oxide phosphors is due in part to the poor crystallinity of the films used. High temperature processing (annealing) of the phosphors will improve the crystal structure and increase the device brightness. This has been demonstrated by Miyata *et al.* [5].

## 1.1 AlInN as an ACTFEL Phosphor

One material system that holds promise as an ACTFEL phosphor is AlInN. Kido *et al.* [8] have demonstrated that GaN, AlN, and $Al_{0.35}Ga_{0.65}N$ can be used to make moderately efficient ACTFEL phosphors. AlInN has certain advantages over AlGaN that suggest that it would to be an even better phosphor candidate. While both materials use trivalent luminescent impurities and, thus, avoid the problems associated with valence compatibility when the luminescent impurity substitutionally replaces the column III cation, the atomic size of the cation strongly favors AlInN. Indium has a significantly larger ionic radius than gallium (0.81 Å versus 0.62 Å). The luminescent impurities most frequently used (europium for red, terbium for green, thulium for blue) have ionic radii between 0.87 Å and 0.95 Å and would more likely occupy substitutional In rather than Ga or Al sites within the lattice. A close match between the atomic radii of the phosphor cation and the substitutional luminescent impurity is essential for minimizing distortion of the crystalline lattice structure. A less distorted lattice implies better crystallinity and improved transport of carriers through the material, resulting in more impact excitations of the luminescent impurities and, hence, more light produced. A second advantage of AlInN

over AlGaN is the larger difference in energy bandgaps of AlN and InN versus AlN and GaN. This should allow for better control in adjusting the compound's bandgap by changing the ratio of Al to In.

The goal of this thesis is to evaluate AlInN as an ACTFEL phosphor candidate and to fabricate a bright ACTFEL device using AlInN as the phosphor. The outline of this thesis is as follows. Chapter 2 is a review of ACTFEL devices: their structure, fabrication, and processing techniques including the topics of sputtering and annealing, operation and physics, electrostatics, and electrical characterization. Chapter 3 describes the experimental techniques used to fabricate and characterize the materials and devices used in this thesis. Chapter 4 presents the experimental results obtained while Chapter 5 gives the conclusions and recommendations for future work.

# CHAPTER 2 - ACTFEL DEVICE LITERATURE REVIEW

This chapter presents a literature review of ACTFEL devices. ACTFEL device structures and materials are reviewed along with fabrication techniques. Operation of ACTFEL devices is discussed as the relevant device physics and electrostatics are presented. Finally, the methods used to electrically characterize ACTFEL devices are presented.

## 2.1 ACTFEL Device Structure

The structure used by Inoguchi *et al.* [1] is the double-insulator-layer structure shown in Fig. 2-1. The advantages of this structure include the protection of the phosphor from moisture and electrical breakdown, as provided by the insulators, and the storage of polarization charge at the phosphor/insulator interface which increases the internal electric field and, hence, increases the device brightness.

There are very specific material requirements for each of the different layers. The glass substrate must be resistant to softening at high temperatures, have a high electrical resistance, and have a coefficient of expansion similar to the conductors, insulators, and phosphors deposited onto it. Typically, Corning 7059 glass has been used, although higher temperature glasses are available. The front conductor must have a very low resistance and be optically transparent. Indium tin oxide (ITO) is used frequently for this layer. Both the front and rear insulators have the same requirements. These include a large electrical breakdown field, high dielectric constant, and optical transparency. The large breakdown field protects the phosphor from catastrophic breakdown while the high dielectric constant produces the high electric fields required in the phosphor at lower externally applied voltages. The insulators must be transparent to allow the light generated in the phosphor to exit the device. Barium tantalate (BTO) and aluminum

titanium oxide (ATO) are used often as ACTFEL insulators. The rear conductor differs from the front conductor in one significant property; it must be highly reflective to redirect any photons travelling toward the rear to the front of the device. The phosphor also has very specific material requirements. It must emit light under high electric fields and not catastrophically break down. ACTFEL phosphors typically operate at electric fields of 1 - 3 MV/cm. The phosphor's emission color is determined by the type of luminescent impurity added. ZnS is the dominant ACTFEL phosphor used today and it produces yellow light when doped with manganese or green light when terbium is used as the impurity.

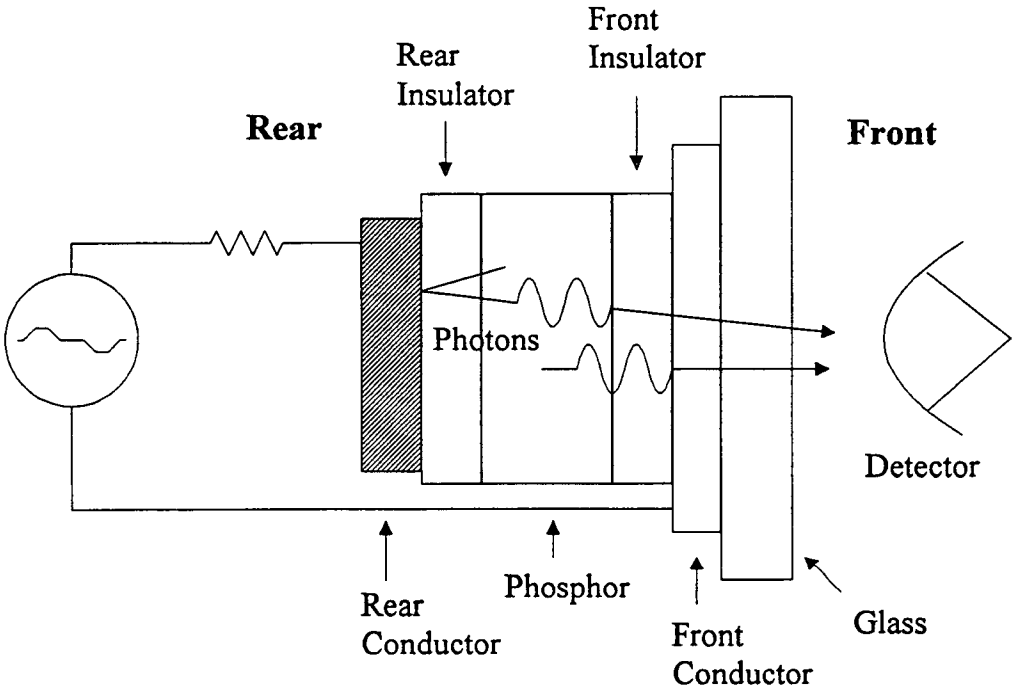


Figure 2-1. A double-insulator-layer ACTFEL device structure.

## 2.2 ACTFEL Device Fabrication and Processing

Modern ACTFEL device fabrication is a series of depositions followed by photolithography to pattern the layers into rows, columns, peripheral devices, or picture elements (pixels).

Depositions are perfomed using several different methods. These include physical vapor deposition (PVD) methods such as electron beam deposition and sputtering, and chemical vapor deposition (CVD) methods like atomic layer epitaxy, metal-organic CVD, and halide-transport CVD. Electron beam deposition (EBD) is accomplished by directing a flow of high energy electrons onto a solid material which evaporates and deposits onto the substrate. Sputtering involves creating a plasma of energetic ions which strike a target, ejecting atoms which deposit onto a substrate. This method offers a high deposition rate and the ability to deposit materials other methods cannot, but the stoichiometry of the sputtered film may not match that of the target. Sputtering is the deposition method used in this thesis and will be reviewed in greater detail below. Atomic layer epitaxy (ALE) is a method in which saturated atomic layers are deposited sequentially. This results in films with excellent stoichiometry and a polycrystalline or amorphous crystal structure, but it has a very slow deposition rate and is not applicable for a wide range of materials. Metal-organic chemical vapor deposition (MOCVD) utilizies metal-organic reactants while halide-transport chemical vapor deposition (HTCVD) uses a halide (typically HCl) to react with Zn to produce ZnCl, which then reacts with $H_2S$ to form ZnS. Both CVD methods offer advantages over ALE such as higher deposition rates and higher luminous efficiencies [9,10].

All of the above deposition methods have certain advantages, but sputtering is best suited for the phosphor development pursued in this thesis. Sputtering requires a target containing the material or compound to be deposited. The materials are usually available as powders, either elementally or in a compound form. The materials can be combined

stoichiometrically and pressed into targets using a hydraulic press located on campus at OSU. (The fabrication of targets is presented in Section 3.1.1.) This is very economical as only a small quantity of a material is required (typically 5 grams or less.) The CVD methods are less desirable for early-stage phosphor development as they require gaseous sources or liquids heated to produce vapors. Materials may not be available in these forms, may come in much larger quantities than desired (gas bottles or liquid flasks), or may not be available to the appropriate degree of purity desired.

Sputtering does have disadvantages but most of these can be overcome. Not all materials can be formed into targets with our present capabilities. Generally, metallic mixtures press well but some oxide and nitride compounds tend to disintegrate after pressing. This limits the range of materials that can be evaluated for ACTFEL devices. The stoichiometry of films deposited by sputtering may vary from that of the target. Oxide and nitride compound targets tend to produce oxygen- or nitrogen-deficient films. This can be compensated for by adding small amounts of $O_2$ or $N_2$ to the chamber during the deposition. The gases are then incorporated into the film and produce the desired stoichiometry. Sputtering in the presence of a reactive gas (such as nitrogen) is referred to as reactive sputtering. Sputter deposition rates are sometimes low, which can lead to undesirable incorporation of oxygen into the films. Finally, sputtering can also damage the lattice of the film, resulting in an amorphous film with a large density of defects. The amorphous nature of the film leads to poor transport of carriers, resulting in less light emission from the ACTFEL device.

Sputtering is the process of striking a target with ions to remove material for deposition onto a substrate. Both ions and energetic electrons are created in the plasma. Argon is frequently used as the sputtering gas. An electric potential is applied across electrodes creating an electric field. Electrons emitted from the electrodes create the ions by collision with the gas atoms, and these positively charged ions are accelerated in the field. The ions strike the target surface and knock out atoms from the target due to their

large kinetic energies. The ejected atoms travel away from the target and can deposit on a substrate surface if they reach it. If the target is a compound, a stoichiometrically similar film, which can be adjusted as necessary by the addition of gases to the argon flow, will deposit onto the substrate. However, the deposited film may not be crystalline due to the destruction of the lattice from the kinetic energies of the incoming atoms. The damage done to the lattice can by repaired, however, by a process known as annealing.

Annealing is the subjection of a material to a high temperature. Lattices with defects and dislocations may rearrange themselves into more perfect structures with the introduction of thermal energy. The temperature at which the crystal lattice begins to recrystallize is referred to as the recrystallization temperature. This is a material parameter unique to each compound.

Post-deposition annealing has been used by several researchers to improve ACTFEL device brightness. Miyata *et al.* [5] reported luminescence after annealing at temperatures above 700 C. Nguyen [7] reported no luminescence prior to annealing, but obtained luminescence after annealing at 500 C.

Photolithography is the patterning of a light-sensitive organic molecule (photoresist or PR) using a mask to create regions in which the PR is chemically resistant to etching as well as regions which can be easily etched. This allows the selective removal of regions of the deposited layer resulting in features on the substrate. The reader is directed to references such as Sze [11] for more specific details of photolithography used in silicon processing, which is similar to ACTFEL processing. (Information on processing used by ACTFEL manufacturers today is mostly proprietary.)

## 2.3 ACTFEL Device Operation and Physics

To produce light from an ACTFEL device, a bipolar-pulse voltage waveform is applied. A typical waveform used is shown in Fig. 2-2. When the magnitude of the

applied voltage is sufficiently large, light is emitted from the device. This minimum voltage required to produce light is called the threshold voltage. As the magnitude of the voltage is increased above the threshold voltage, the intensity of the emitted light increases. This can be seen from a plot of luminescence versus voltage, as shown in Fig. 2-3. Note that the threshold voltage can be read directly from this plot.

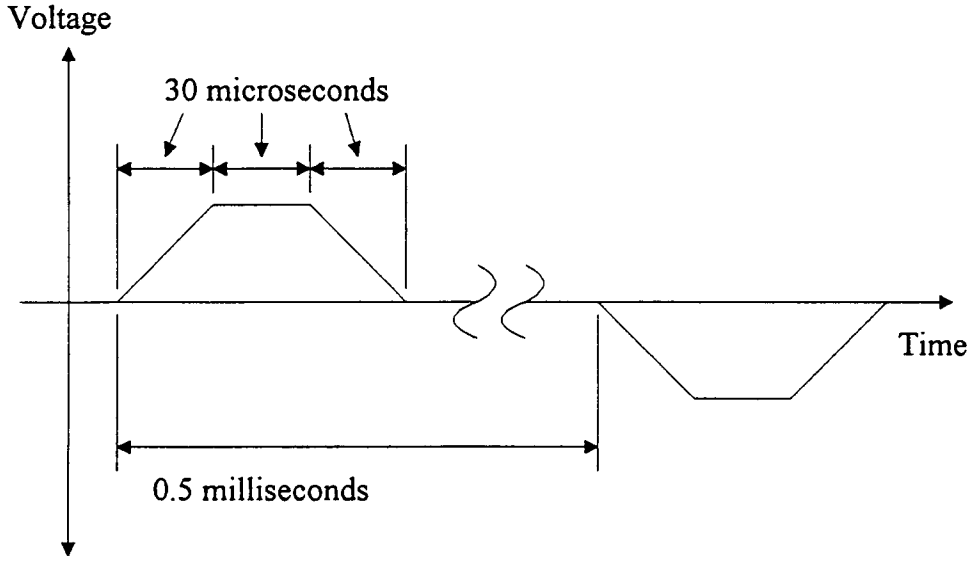


Figure 2-2. A typical ACTFEL device voltage waveform.

The conventional ACTFEL device physics theory used to explain the light emission process is as follows. As the applied voltage is increased, electrons in the phosphor are promoted from interface states into the conduction band. The high electric field present in the phosphor accelerates the electrons which are transported across the phosphor layer. These carriers can impact excite the luminescent impurities. The decay of the excited luminescent impurity electrons back to their ground states produces light with a wavelength characteristic of the energy difference between the ground and excited energy states. However, the excited luminescent impurity electrons may also decay non-radiatively, in which case no light is produced (the excess energy is dissipated as

phonons.) Eventually, the electrons are captured in interface states at the phosphor/insulator interface where they wait for the next voltage pulse to repeat the cycle.

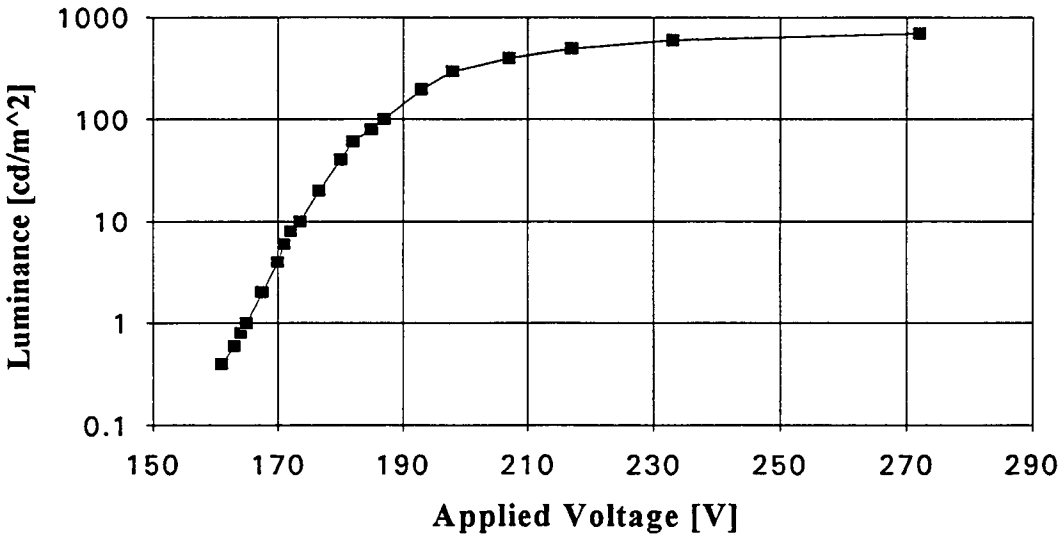


Figure 2-3. A typical ACTFEL device luminance-voltage plot (from Mikami *et al.* [9]).

An energy band diagram of a double-insulator-layer ACTFEL device is shown in Fig. 2-4. The interface state density and energy depth vary with the phosphor and insulator and are not known exactly. As a pulsed voltage waveform is applied to the device, the band bending changes accordingly. The cycle of changes in the energy band is shown in Fig. 2-5.

Figure 2-5a shows the beginning of the cycle. As the external voltage is applied (positive with respect to the rear conductor, negative with respect to the front conductor), electrons are emitted from interface states into the phosphor conduction band. There are three possible mechanisms for electron emission from interface states: thermal emission, pure tunneling, or phonon-assisted tunneling [13]. The electrons accelerate and impact excite the luminescent impurities. Light is produced from radiative relaxation of the

excited electrons. Subsequently, the electrons are driven to the phosphor/insulator interface on the front conductor side and are trapped in interface states. The current flow across the phosphor is referred to as conduction current.

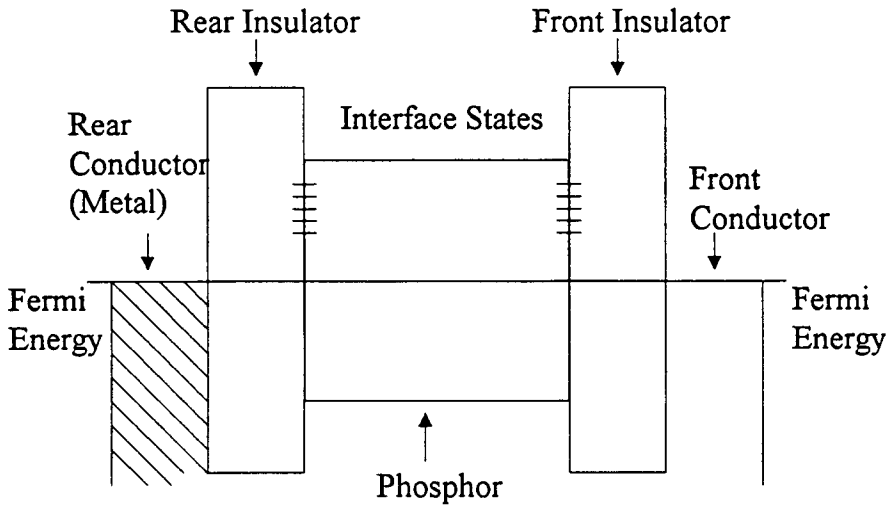


Figure 2-4. A double-insulator-layer ACTFEL device energy band diagram.

When the positive voltage is removed, the Fermi level voltage separation is reduced to zero. This is shown in Fig. 2-5b. Because of electron transfer, a net negative charge appears at the rear conductor side phosphor/insulator interface and a net positive charge appears at the front conductor side phosphor/insulator interface. This charge is called polarization charge. It induces a field in the phosphor even though no external voltage is applied.

When the external voltage becomes negative, a similar process occurs. This is shown in Fig. 2-5c. Electrons are emitted from the rear conductor side phosphor/insulator interface into the phosphor conduction band. The polarization charge created during the previous pulse now decreases the external voltage which must be applied to begin the electron injection process. The electrons accelerate and impact excite the luminescent impurities. Light is emitted and conduction current flows in the opposite direction to that

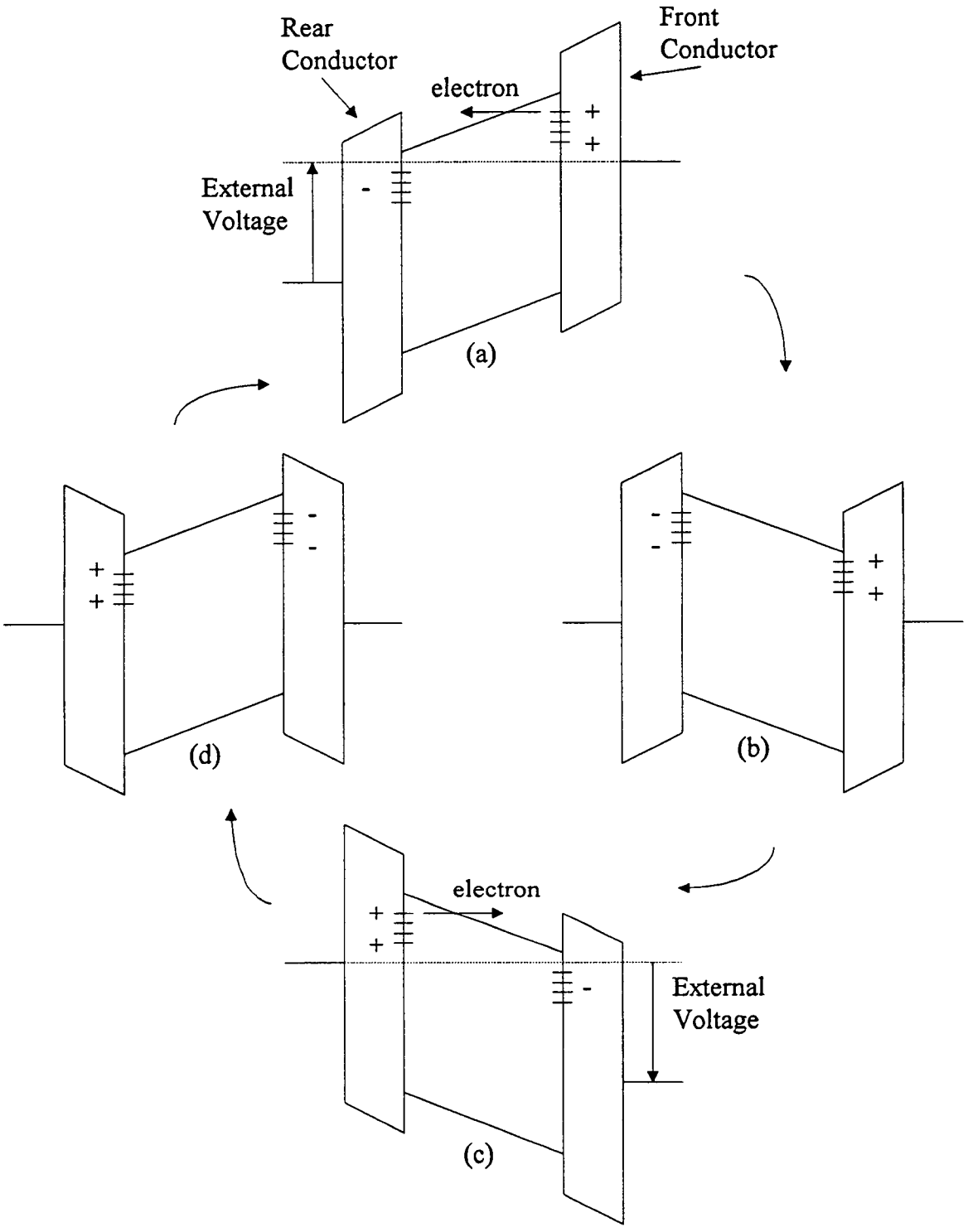


Figure 2-5. A typical ACTFEL device energy band cycle (after Douglas [12]).

of the previous pulse. Electrons are eventually collected at the front conductor side phosphor/insulator interface.

As the external voltage goes to zero following the negative pulse, polarization charge appears again but with an opposite polarity as for the positive pulse. This is shown in Fig. 2-5d.

## 2.4 ACTFEL Device Electrostatics

Two physical quantities that are used frequently to characterize ACTFEL devices are the internal charge, $Q_{int}$, and the phosphor electric field, $F_p$. Analytical expressions for these quantities are developed by Bringuier [14].

To derive expressions for these quantities in terms of measurable values, one must begin with Gauss' Law which relates the electrical flux crossing any closed surface to the charge enclosed by that surface. If one assumes uniform electric fields (no bulk charge) perpendicular to the interface, one can describe the insulator and phosphor charges, respectively, as

$$Q_i = \varepsilon_o \varepsilon_i F_i \qquad (2 - 1)$$

$$Q_p = \varepsilon_o \varepsilon_p F_p \qquad (2 - 2)$$

where $\varepsilon_o$ is the permittivity of free space, $\varepsilon_i$ and $\varepsilon_p$ are the dielectric constants for the insulator and phosphor, respectively, and $F_i$ and $F_p$ are the insulator and phosphor electric fields. One can define the internal charge $Q_{int}$ as the charge trapped between the insulator and phosphor layers, given by

$$Q_{int} = Q_i - Q_p = \varepsilon_o \varepsilon_i F_i - \varepsilon_o \varepsilon_p F_p. \qquad (2 - 3)$$

Also, one can express the voltage applied across the device, $V_a$, as

$$V_a = d_i F_i + d_p F_p \qquad (2 - 4)$$

where $d_i$ and $d_p$ are the insulator and phosphor thicknesses, respectively.

The applied voltage $V_a$ can be measured directly, but the internal charge $Q_{int}$ cannot. However, $Q_i$ can be measured by using an appropriately sized capacitor in a Sawyer-Tower configuration (i.e. a capacitor in series with the ACTFEL device). $Q_i$ is then given by

$$Q_i = C_s V_s \qquad (2 - 5)$$

where $C_S$ is the Sawyer-Tower capacitor and $V_S$ is the voltage dropped across this capacitor. Using this equation for $Q_i$, one can solve for the internal charge and the phosphor electric field

$$Q_{int} = \frac{C_i + C_p}{C_i} Q_i - C_p V_a \qquad (2 - 6)$$

$$F_p = \frac{1}{d_p}\left[V_a - \frac{Q_i}{C_i}\right] \qquad (2 - 7)$$

where $C_i$ and $C_p$ are the insulator and phosphor capacitances per unit area. $C_i$ and $C_p$ can be expressed as

$$C_i = \frac{\varepsilon_o \varepsilon_i}{d_i} \qquad (2 - 8)$$

$$C_p = \frac{\varepsilon_o \varepsilon_p}{d_p}. \qquad (2 - 9)$$

## 2.5 ACTFEL Device Electrical Characterization

There are a variety of methods used to electrically characterize ACTFEL devices. Two methods of particular interest use the quantites $Q_i$, $Q_{int}$, and $F_p$ developed in the previous section. They are the charge-voltage ($Q_i$-$V_a$) method [15] and the internal charge-phosphor field ($Q_{int}$-$F_p$) method [16]. Plots generated via these methods provide much information about charge transfer within the devices, the phosphor field strengths, and non-ideal behavior such as leakage currents and charge relaxation.

Figure 2-6 shows the voltage waveform used to test ACTFEL devices with the various points of interest in the period labeled **A** through **J**. The changes in voltage correspond to different points on the $Q_i$-$V_a$ and $Q_{int}$-$F_p$ plots.

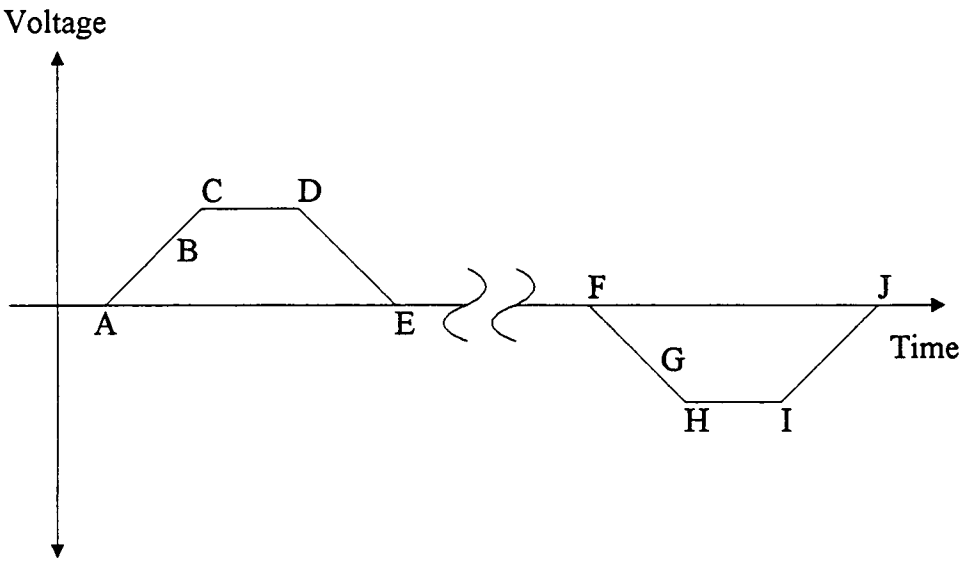


Figure 2-6. Points of interest on the ACTFEL device voltage waveform.

Figure 2-7 shows a typical ACTFEL device $Q_i$-$V_a$ plot. (Note that this plot and the subsequent $Q_{int}$-$F_p$ plot are obtained at steady-state and not from an initial transient.) At the beginning of the positive pulse (point **A**), the applied voltage is zero but the charge

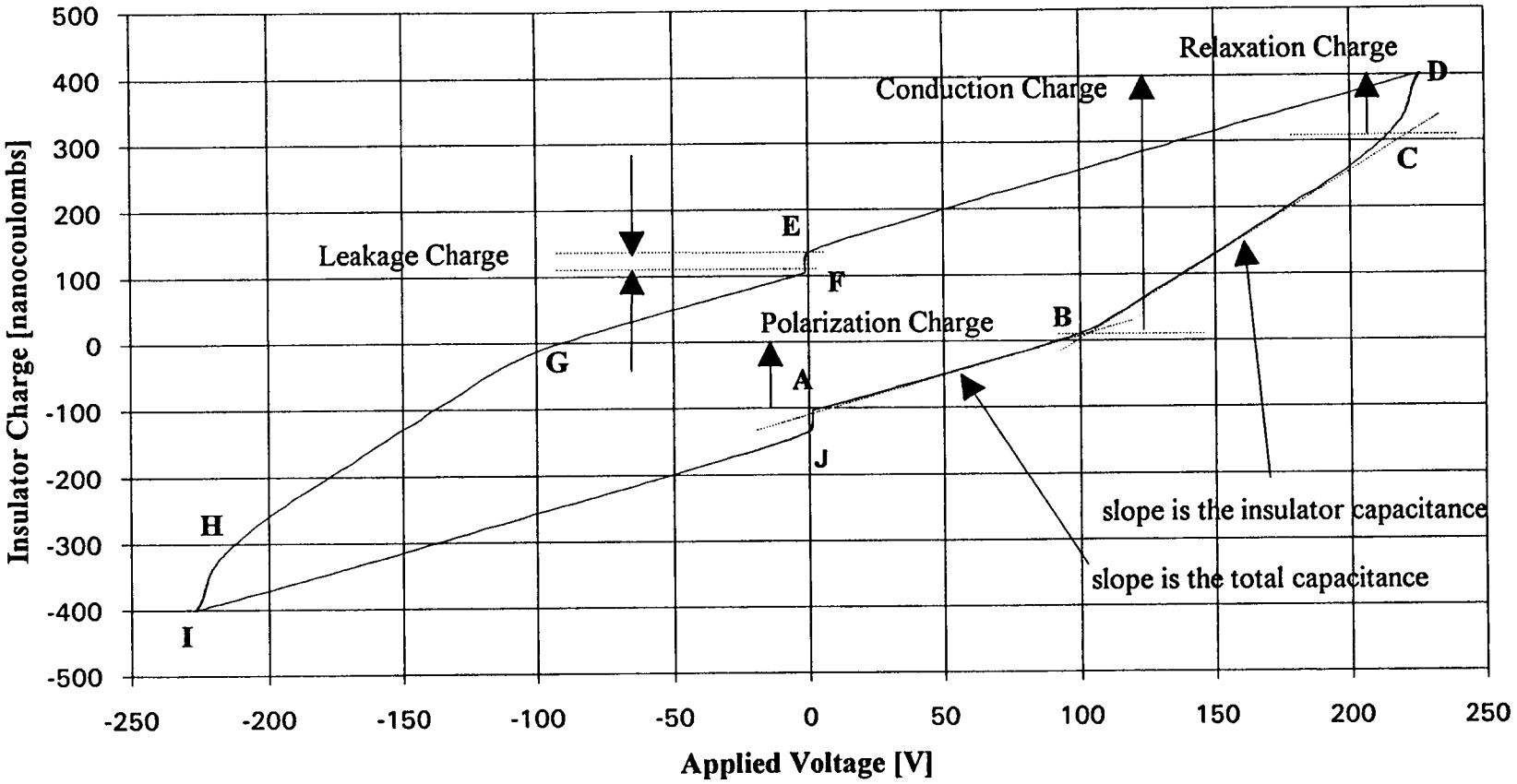


Figure 2-7. A typical ACTFEL device $Q_i$-$V_a$ plot.

is not. This is the polarization charge mentioned earlier. Once the positive pulse begins, the magnitude of $Q_i$ decreases as the electric field increases. Point **B** shows the turn-on voltage. At this point electrons begin to tunnel from interface states into the phosphor conduction band. The turn-on voltage differs from the threshold voltage because of the polarization charge which reduces the turn-on voltage below that of the threshold voltage. The turn-on voltage can be thought of as a steady-state threshold voltage.

At point **C**, the applied voltage reaches its maximum. Some additional charge transfer occurs from **C** to **D**, the end of the maximum applied voltage. As the applied voltage decreases, the charge is reduced. At point **E**, the applied voltage becomes zero. A certain amount of charge is lost because of the non-zero phosphor electric field. The amount of charge lost is referred to as the leakage charge and can be read directly from the plot.

The negative pulse of the waveform is analogous to the positive pulse. The difference between the two is the opposite polarity of the charges and voltages.

Figure 2-8 shows a typical ACTFEL device $Q_{int}$-$F_p$ plot. At point **A**, the polarization charge can be read directly from the plot. As the voltage is increased, the phosphor field increases but $Q_{int}$ remains constant. When the turn-on voltage is reached, tunneling of electrons from the interface states is shown clearly in the plot as $Q_{int}$ decreases. The plot shows a fairly constant $F_p$ between points **B** and **C**. This is called the steady-state phosphor field, $F_{ss}$.

As the maximum applied voltage is reached at point **C**, the internal charge continues to increase as additional electrons are emitted but $F_p$ decreases. This is referred to as relaxation. The relaxation charge can be read directly from either a $Q_i$-$V_a$ or $Q_{int}$-$F_p$ plot.

After point **D**, the applied voltage decreases. The leakage charge shown in a $Q_i$-$V_a$ plot also can be seen in a $Q_{int}$-$F_p$ plot. The total charge transfer during a pulse

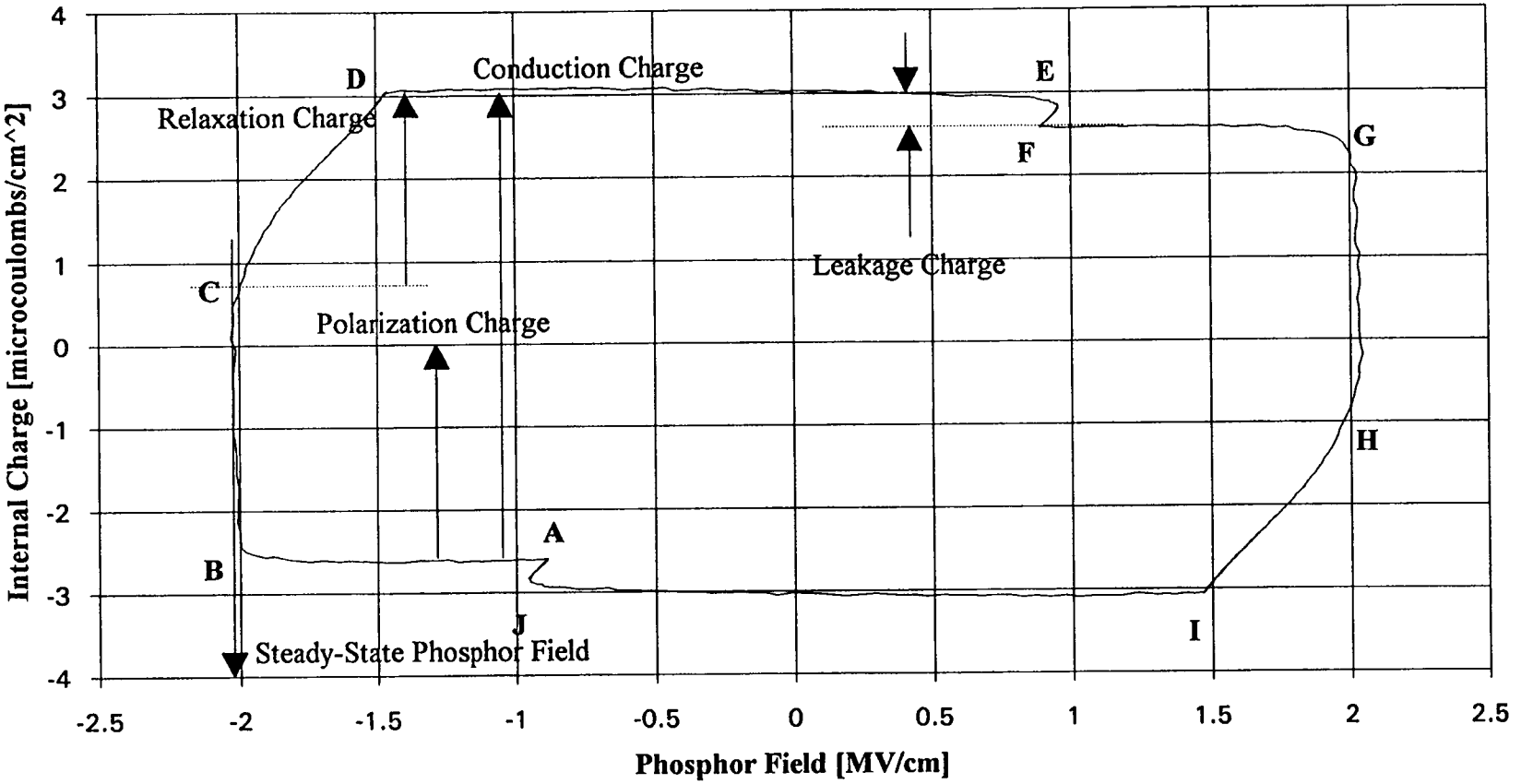


Figure 2-8. A typical ACTFEL device $Q_{int}$-$F_p$ plot.

(between points **A** and **E** or **F** and **J**) is called the conduction charge, and can be measured from either a $Q_i$-$V_a$ or a $Q_{int}$-$F_p$ curve.

The negative pulse of the waveform for a $Q_{int}$-$F_p$ plot is analogous to the positive pulse; the difference between the two is the opposite polarity of the charges and fields.

To generate the $Q_{int}$-$F_p$ plot, the capacitances of the insulator and phosphor layers must be known. These can be difficult to calculate due to inaccuracies in the dielectric constant measurement, the film thickness, and the device area. The total capacitance and insulator capacitance can be determined from the slopes of different parts of the $Q_i$-$V_a$ curve. A more common method, however, is the capacitance-voltage (C-V) method [17].

The C-V method is based on the equation

$$C(V_a) = \frac{i(t)}{d V_a / dt} . \qquad (2 - 10)$$

The ACTFEL device current i(t) is given by Ohm's Law,

$$i(t) = \frac{V_s(t)}{R_s} \qquad (2 - 11)$$

where $V_S(t)$ is the voltage dropped across a sense resistor, $R_S$. The time rate of change in the voltage across the ACTFEL device, $dV_a(t)/dt$, is calculated numerically.

A typical ACTFEL device C-V plot is shown in Fig. 2-9. Note that the initial capacitance is the series combination of the insulator and phosphor capacitances. As the voltage across the device increases, the phosphor layer breaks down and stops behaving like a capacitor. As a result, the measured capacitance is the insulator capacitance.

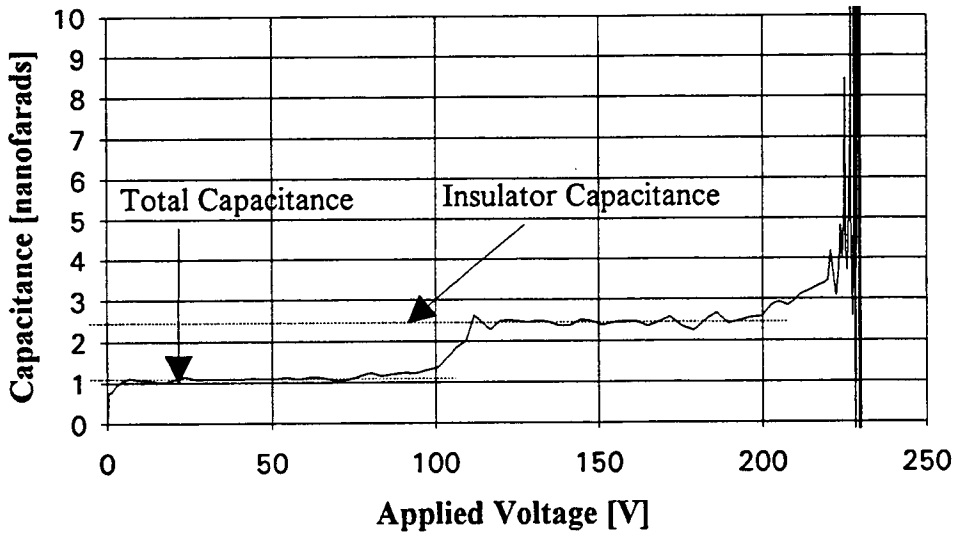


Figure 2-9. A typical ACTFEL device C-V plot.

# CHAPTER 3 - EXPERIMENTAL TECHNIQUES

This chapter presents the experimental techniques used to deposit and process the phosphor, characterize material parameters of the phosphor, and characterize full ACTFEL devices. First, target fabrication and the sputtering system used are discussed, followed by a description of the various measurements taken to characterize the phosphor film. Finally, the techniques used to develop and characterize full ACTFEL devices are presented.

## 3.1 Phosphor Deposition and Processing

### 3.1.1 Target Fabrication

Sputtering requires a material to be sputtered. A target containing the material to be sputtered first must be fabricated. This requires obtaining the individual compounds that will be pressed into the target in a very fine powder form. The compounds are weighed to produce the desired composition and mixed thoroughly. The target powder is placed into a stainless steel mold and pressed using a load of 5 tons to produce the target. The target's size is 1 1/4" in diameter and approximately 1/8" thick. The target is then mounted on a 3" diameter aluminum plate and placed in one of the RF sputtering system's magnetron guns.

### 3.1.2 The RF Sputtering System

An RF sputtering system is used to deposit all the phosphor films described in this work. The system used is described thoroughly by Ang [6] but the system's features are reviewed briefly.

The RF sputtering system features a deposition chamber housing two 3" RF magnetron sputtering guns. The system is capable of depositing one film and then a second film using the other sputter gun. The guns are water-cooled and linked to an RF matching network and an RF generator. A diffusion pump and mechanical pump maintain pressures from microtorr to millitorr. A throttle valve is use to adjust the deposition pressure. The system is plumbed with argon, nitrogen, and a dilute nitrous oxide mixture (5 % $N_2O$ and 95 % He).

The substrates are introduced into the deposition chamber via a loadlock. A substrate is mounted vertically onto a substrate holder, placed into the loadlock, and the loadlock is roughed to a pressure approximately equal to that of the deposition chamber. A gate valve connects the two chambers. The gate valve is opened and the substrate holder is transferred from the loadlock to the deposition chamber via a chain belt.

For this work, a substrate heater was built and installed in the system. It consists of a nichrome wire mounted in a stainless steel box suspended from the deposition chamber's ceiling. The heater is suspended directly in front of a sputter gun, and the substrate holder travels between the heater and the gun. A current is passed through the wire, producing heat from the wire's resistance ($I^2R$ heating). The heater produces substrate temperatures up to 200 C during deposition. The heater is capable of producing higher temperatures but is limited to 200 C due to the close proximity of o-ring seals and possible warping of the substrate holder and the glass viewport.

### 3.1.3 Deposition Parameters

There are a number of parameters to be set during a deposition. They include process gas types and flow rates, deposition pressure, deposition power, and substrate temperature.

Gas flows are selected and set using mass flow controllers (MFCs). Any combination of Ar, $N_2$, and $N_2O$ may be used. The upper limit of the gas flow rates is set by the diffusion pump's throughput. Once the pump's throughput has been exceeded, a stable pressure in the deposition chamber cannot be maintained.

Deposition pressure is set by adjusting the throttle valve's position. The throttle valve is located between the deposition chamber and the diffusion pump.

Deposition power is set directly at the RF generator. Increasing the power increases the amplitude of the voltage waveform produced by the generator, which in turn increases the sheath potential. The power is limited by the heating that occurs in the target. If the deposition power is too high, the target will melt.

Substrate temperature is set with the power setting on a rheostat providing the current to the nichrome wire. The substrate temperature is proportional to the current flow through the wire. Substrate temperature is not measured directly during depositions due to the inability to connect a thermocouple to the substrate holder after it passes from the loadlock to the deposition chamber via the gate valve. Calibration curves are generated for substrate temperatures as a function of rheostat setting and a function of time. Using these curves, estimates are made for the deposition temperature and for the time required for the substrate to reach 90 % of the final substrate temperature.

### 3.1.4 Annealing

Films can be processed further after deposition with a rapid thermal processor (RTP) to rapidly heat and cool the substrate. The system used is an RX series RTP from AET Thermal. The system is capable of anneals from 400 C to 1100 C for times (at maximum temperature) as short as 10 seconds to anneals of several minutes, in an ambient of forming gas (4 % $H_2$ and 96 % $N_2$).

A 2" Lindberg furnace can also be used for annealing substrates. It is capable of annealing temperatures from 400 C to 950 C for anneals of a few minutes to several hours. The furnace uses the same forming gas ambient as the RTP.

### 3.1.5 Metallization

Following deposition and annealing (if desired), some substrates are metallized using a Veeco evaporation system so that various electrical measurements can be performed. Stencils of thin metal with either a C-V or full device pattern are used to produce a pattern on the substrate. A CV pattern consists of an 11 x 11 matrix of Al dots with an area of 0.011 $cm^2$ and a full device pattern consists of a 2 x 5 matrix of Al dots with an area of 0.079 $cm^2$. Aluminum layers of approximately 2000 Å are used.

## 3.2 Film Characterization

There are several techniques used to evaluate the phosphor thin films. They include physical, electrical, and optical measurements. The different techniques and their requirements are presented below.

### 3.2.1 Physical Measurements

The two physical measurements used to characterize the thin films are the deposition rate and the refractive index, $n$. The deposition rate is determined by dividing the deposited thickness by the deposition time. There are two distinctly different methods, however, for measuring the deposited thickness. They are ellipsometry and a step height measurement with a stylus. Ellipsometry requires depositions onto a silicon wafer while step measurements can be performed on any substrate (Si or glass). Films of 1000 Å or

less are used for ellipsometry to avoid problems with convergence to the correct film thickness. A step is produced by covering part of the substrate with either adhesive tape or aluminum foil prior to deposition and removing the covering afterwards. A Gaertner Scientific Instruments model L116A ellipsometer is used for the ellipsometer measurements and a Tencor Instruments Alpha-Step 100 is used for the step height measurements. The refractive index is measured with the ellipsometer for films deposited onto Si.

### 3.2.2 Electrical Measurements

There are three thin-film parameters that are derived from electrical measurements. They are the film's dielectric constant, bulk resistivity, and breakdown field. All three measurements are taken on glass substrates with a conductive layer, which are metallized after deposition using a C-V patterned stencil. (In this work, ITO is used for the conductive layer. Such substrates are referred to hereafter as ITO substrates.) Deposited phosphor film thicknesses of 2500 Å are used. The substrate and film can be annealed, if desired, prior to metallization. ITO can be deposited onto a higher-temperature NEG glass if higher temperatures are required.

The dielectric constant is obtained from capacitance measurements of the Al dots on the ITO substrate. A Hewlett-Packard 4275A Multifrequency LCR meter is used for these measurements. The dielectric constant, $\varepsilon_p$, is found from

$$\varepsilon_p = \frac{Cd}{\varepsilon_o A} \qquad (3 - 1)$$

where C is the capacitance of the dot, d is the film thickness, and A is the dot area. $\varepsilon_p$ is evaluated at 10 kHz.

The bulk resistivity is obtained by measuring the current flow across the device at a given voltage. A Hewlett-Packard 4140B pA meter / DC voltage source is used for these measurements. For consistency, the measurement is taken at a voltage corresponding to a field of 1 MV/cm across the phosphor. (This voltage is obtained by multiplying the film thickness by 1 MV/cm.) The resistance R is given by Ohm's Law,

$$R = \frac{V}{I} \qquad (3 - 2)$$

where V is the voltage required to produce a 1 MV/cm field within the phosphor and I is the current at this voltage. The bulk resistivity $\rho$ is given by

$$\rho = \frac{RA}{d} \qquad (3 - 3)$$

where R is the resistance, A is the dot area, and d is the film thickness.

The breakdown field is also measured with the Hewlett-Packard 4140B. The voltage across the device is increased slowly and the current is monitored. When the current exceeds $10^{-4}$ A, the applied voltage is defined to be equal to the breakdown voltage. The breakdown field is the breakdown voltage divided by the film thickness. Note that this is not a catastrophic breakdown but simply a measure of an acceptable magnitude of current at a given field.

### 3.2.3 Optical Measurements

There are two optical methods used to evaluate the deposited films. They are absorption and photoluminescence.

Absorption measurements are used to calculate the optical bandgap of a material. These measurements are taken using a Hewlett-Packard 8452A Diode Array Spectophotometer. The measurement requires deposition onto a glass or a quartz

substrate. Deposited film thicknesses of 3000 Å are used. The absorption coefficient $\alpha$ is related to the absorbance $A_{abs}$ by

$$\alpha = \frac{A_{abs}}{d} \qquad (3 - 4)$$

where d is the film thickness. Using the absorption coefficient and the corresponding wavelength's energy E, a Tauc plot can be obtained by plotting $\sqrt{\alpha E}$ versus E. The x-axis intercept of a Tauc plot yields $E_{opt}$, the optical bandgap.

Photoluminescence (PL) is used to evaluate a deposited film for brightness and light color. An Ultra-Violet Products UVG-54 shortwave UV lamp is used for this. Films deposited onto a Si or a glass substrate, annealed or as-deposited, are placed under the lamp and evaluated visually. Note that although this is a qualitative measurement, it allows for direct, side-by-side comparisons which can be performed quickly and easily.

## 3.3 Device Characterization

There are several techniques used to evaluate ACTFEL devices. They include electrical and optical measurements. The different techniques are presented below.

### 3.3.1 Electrical Characterization

The electrical techniques used to characterize ACTFEL devices include the C-V, $Q_i$-$V_a$, and $Q_{int}$-$F_p$ methods. To generate these plots, measurements are taken using the setup shown in Fig. 3-1. Measurements are taken on films deposited on a substrate consisting of NEG (high temperature) glass, a conductive layer, an insulating layer, and a thin layer of ZnS. (For this work, the conductive layer used is ITO, the insulating layer used is ATO, and the ZnS layer thickness is 300 Å. This substrate is referred to hereafter as a DZA substrate.) Deposited film thicknesses of 4000 Å are used. Using a personal

computer to control the equipment, a waveform is programmed into the generator and supplied to the high-voltage amplifier. This produces the voltages necessary to drive the device. A series resistor of 1 kΩ is used to limit the current and minimize the likelihood of device breakdown, and to protect the high-voltage amplifier if the device breaks down. The waveform is applied across the ACTFEL device. A sense element (either a resistor or a capacitor) is placed in series with the ACTFEL device. An oscilloscope is used to measure the voltages across the ACTFEL device and the sense element, which are stored in the computer. A list of the equipment used is given in Table 3-1.

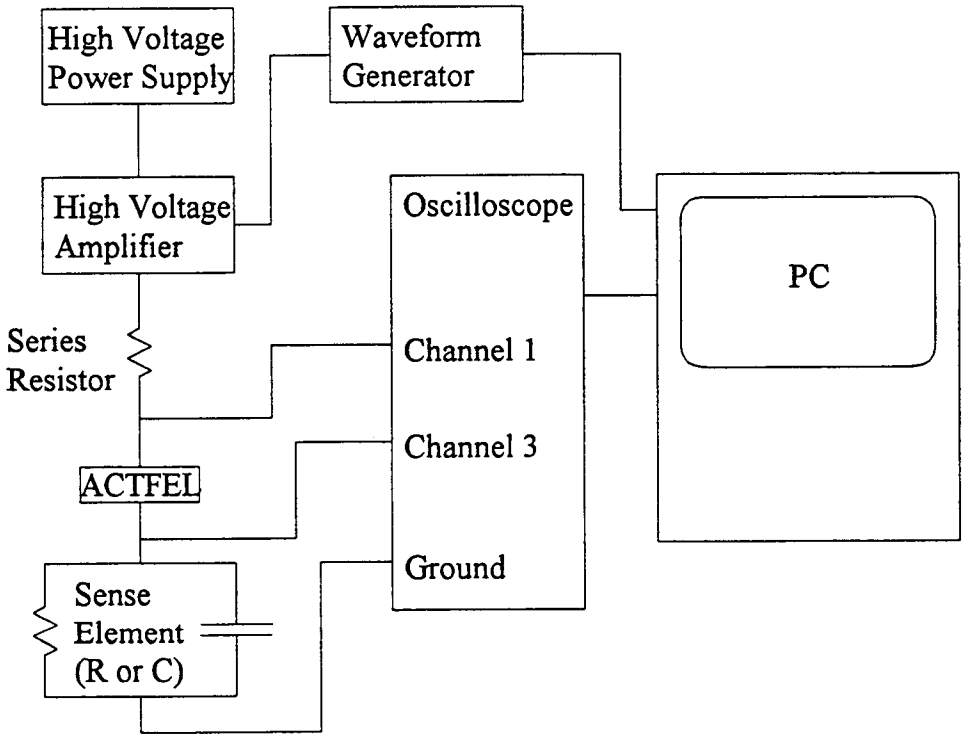


Figure 3-1. Electrical characterization measurement setup.

C-V measurements are obtained using a resistor as the sense element. The value of the resistor used is approximately 10 Ω. Using Eq. 2-10, the measured voltages are manipulated to produce the C-V plot.

Table 3-1 Electrical Characterization Measurement Equipment List

| Equipment | Manufacturer | Model |
|---|---|---|
| High-voltage power supply | Kikusui Electronics Corp. | PAB 350-0.2 |
| High-voltage amplifier | OSU | - |
| Waveform generator | Wavetek | 395 |
| Oscilloscope | Tektronix, Inc. | TDS420 |

$Q_i$-$V_a$ and $Q_{int}$-$F_p$ measurements are obtained using a capacitor as the sense element. The value of the capacitor used is approximately 100 nF. Using Eqs. 2-5, 2-6, and 2-7, the measured voltages are manipulated to produce the $Q_i$-$V_a$ and $Q_{int}$-$F_p$ plots.

### 3.3.2 Optical Characterization

The optical measurements used to evaluate ACTFEL devices are brightness-voltage (B-V) and spectral analysis of the luminescent intensity. These measurements are taken using the setup shown in Fig. 3-2.

The B-V measurement is similar to the C-V measurement. A personal computer programs the waveform into the generator, which is supplied to the high-voltage amplifier and applied across the ACTFEL device. A Pritchard photometer measures the brightness of the ACTFEL device as the waveform's amplitude is increased. No sense elements are required for this measurement. The computer stores the voltage measured across the ACTFEL device and the corresponding brightness.

The spectral analysis measurement is similar to the B-V measurement except that the waveform's amplitude is held constant and the photometer measures the intensity at selected wavelengths across the visible spectrum. (The Pritchard records the brightness integrated across the visible spectrum for the B-V measurement.)

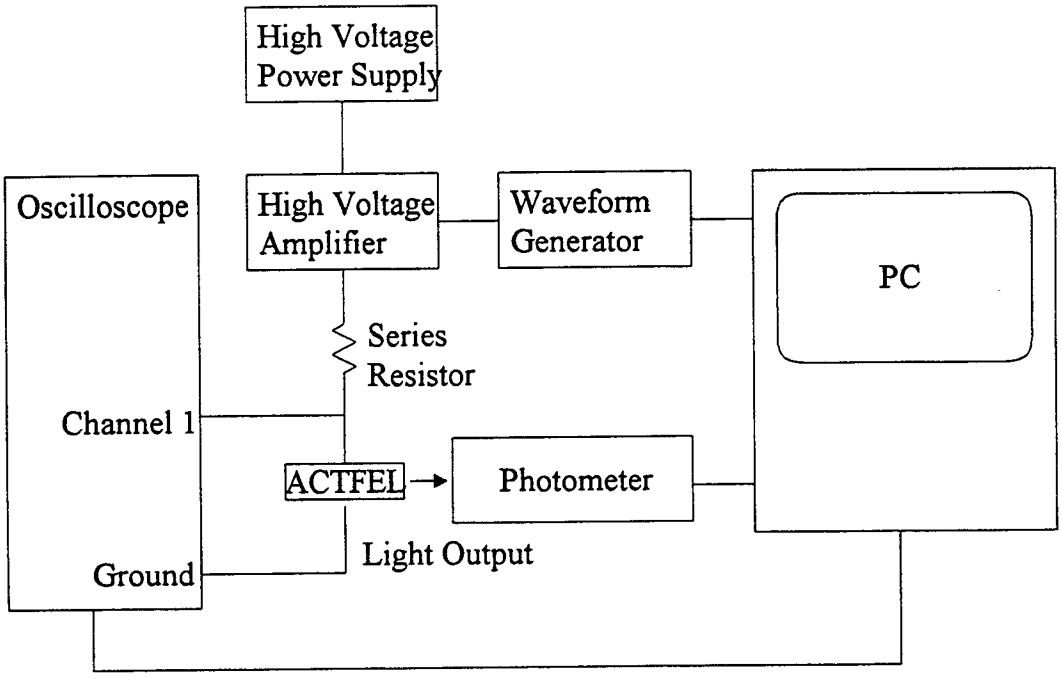


Figure 3-2. Optical characterization measurement setup.

### 3.4 ACTFEL Phosphor Development and Characterization

There is a definite, logical sequence to developing and evaluating ACTFEL phosphors. Material requirements such as transparency, stability, and photoluminescence should be satisfied before electrical and optical parameters can be evaluated and adjusted. Figure 3-3 shows the flowchart used in this work to develop and evaluate ACTFEL phosphors.

The starting point for a phosphor is to press a sputter target. The requirement here is to successfully form a target which does not disintegrate. If the mixture presses, the process of development and evaluation continues. Should the mixture fail to press, a new target is pressed. The possibilities for fabricating a new target include making the mixture more metallic, lowering the oxide/nitride content, using a different pressing technique (such as hot pressing), or purchasing a target from a vendor.

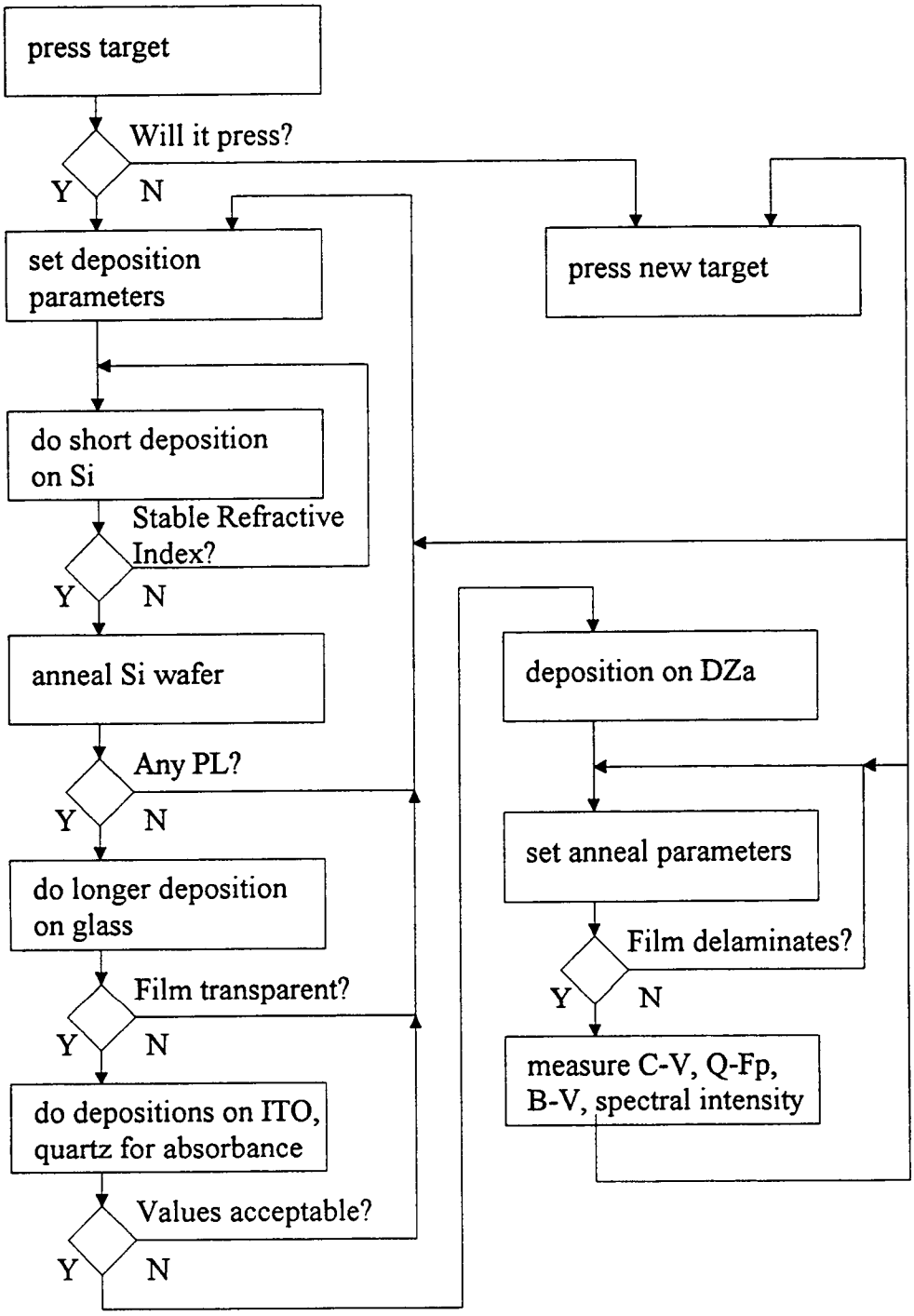


Figure 3-3. The ACTFEL phosphor development flowchart.

The next step in the process is to set the deposition parameters. These include the process gas species and flow rates, the deposition pressure, the deposition power, and the substrate temperature. Once these parameters are set, short depositions onto silicon wafers are performed. The deposition rate is determined along with the refractive index of the film. Depositions are performed repeatedly until a stable film is produced. Several runs are typically required after a process gas flow change or after the machine has been idle for a period of time before a repeatable $n$ is obtained.

Once film stability has been achieved, anneals are performed on the silicon wafers using the RTP. The wafers are evaluated under the UV lamp for PL, noting the brightness and color of the luminescence. A variety of annealing temperatures and times are evaluated. Should these fail to produce PL, the deposition parameters can be adjusted and the loop restarted.

The next step is to perform longer depositions onto glass substrates. The purpose is two-fold. First, it allows for evaluation of the film transparency, something that is difficult to do using a silicon wafer. Second, it allows for a more accurate determination of the deposition rate. A step height measurement is taken on the substrate. Because ACTFEL phosphor depositions are frequently over an hour long, extrapolating a deposition rate based on a deposition time of 20 minutes or less, and using a different substrate, can give misleading results. Again, if the thin-film's transparency is unacceptable, the deposition parameters can be be adjusted and the loop restarted.

With the film stability, PL, and transparency all satisfactory, the thin-film's electrical and optical properties are determined. Electrical measurements are taken on depositions of the film on an ITO layer over glass, while the optical bandgap is determined from absorption measurements taken on the film deposited on glass or quartz.

The electrical parameter of primary interest is the breakdown field $F_{br}$. Should the film break down at less than 0.5 MV/cm or more than 3 MV/cm, the deposition parameters should be adjusted since it is unlikely that the phosphor would break down in an ACTFEL device. This failure to break down would limit the conduction charge, and hence the impact excitation and light emitted from the ACTFEL device.

The remaining electrical parameters, the dielectric constant $\varepsilon_p$ and bulk resistivity $\rho$, are also useful for the assessment of ACTFEL phosphors. The dielectric constant provides a numerical check for later results produced from full devices. Capacitance can be calculated from the dielectric constant using Eq. 3-1 and compared with C-V or $Q_i$-$V_a$ results. The bulk resistivity is closely related to $F_{br}$, since the former is a measure of resistance while the latter is the field required to produce a certain current. $\rho$ is useful for comparison with other ACTFEL phosphors.

The Tauc plot, used to determine the optical bandgap $E_{opt}$, is useful for providing insight into band-tail states present in the phosphor. The curve for energies below the absorption peak should be linear. Deviations from linearity indicate the presence of band-tail states which increase the scattering of electrons. Scattered electrons lose energy and are less likely to impact excite luminescent impurities, thus, reducing the light emission.

Once the electrical and optical parameters are acceptable, full ACTFEL devices are fabricated and annealed. Following annealing, the film is checked for delamination which usually indicates that the annealing temperature is excessive. Once a satisfactory anneal has been determined, the full device is evaluated.

ACTFEL devices are evaluated by techniques including C-V, $Q_i$-$V_a$, $Q_{int}$-$F_p$, B-V, and spectral intensity. The $Q_{int}$-$F_p$ technique is the most useful for assessment of new ACTFEL phosphors. The $Q_{int}$-$F_p$ plot shows whether field clamping occurs within the device, the value of the phosphor field if it clamps, and the amount of conduction charge within the device. Field clamping occurs when the maximum internal electric field for a material is reached and is independent of the maximum voltage of the waveform used.

Empirically, devices which clamp seem to yield the best performance. A low phosphor field prevents electrons from attaining sufficient energy to efficiently impact excite luminescent impurities and produce light. The magnitude of the conduction charge is a useful parameter for assessing progress in the optimization of an ACTFEL phosphor. The amount of light emitted should increase with increasing conduction charge. Since the charge is a measure of the number of electrons transported from one phosphor/insulator interface to the other during a voltage pulse, and light emission is a result of impact excitaion of the luminescent impurities, the light emitted is proportional to the amount of conduction charge present.

A C-V plot is useful for fitting the $Q_{int}$-$F_p$ plot [18] since the latter requires values for $C_i$ and $C_t$ while the former does not require any values to produce a plot. The $C_i$ and $C_t$ values used to obtain a $Q_{int}$-$F_p$ curve can be fit by trial and error, but using values taken from a C-V plot provides greater confidence in the results. $C_i$ and $C_t$ can also be determined from a $Q_i$-$V_a$ plot. C-V plots also produce information about internal processes, such as space charge formation, which are important in subsequent evaluations of an ACTFEL phosphor.

B-V and spectral intensity are also used to evaluate ACTFEL phosphors. B-V plots show whether sharp threshold and saturation voltages are produced. Sharp, well defined voltages are desirable in ACTFEL devices to control the light emission. A step function would be most desirable, such that below the threshold voltage no light is emitted, and above it the light emitted is at 100 % brightness. Least desirable is a ramp function, such that light emission increases linearly with a small slope. Spectral intensity is useful for identifying the intensities of the light emitted at each wavelength. Bright, wide-spectrum light emission can be used with filters to produce the primary colors, but using filters increases ACTFEL device cost and complexity. Narrower spectral emission does not require filtering but may contain significant contributions of two or more colors, making production of full color displays difficult.

After measuring these parameters, three possible courses of action are shown in Fig. 3-3. The first course is to adjust the anneal parameters. Increasing the anneal temperature can increase the conduction charge and possibly improve the ACTFEL device's preformance. The second course is to change the deposition parameters and alter $F_{br}$ and $F_{ss}$. The third course is to press a new target. A point is eventually reached where the limitations of the target are reached, and adjusting the deposition or anneal parameters no longer improves the phosphor's performance.

There are other evaluation techniques used to characterize ACTFEL phosphors which are not shown on the flowchart. These include Auger electron spectroscopy (AES) analysis, x-ray diffraction (XRD), and aging studies. These techniques are not shown because they are typically not performed for every iteration of the loop. AES analysis reveals the elemental composition of a deposited film. This is useful, especially for reactive sputtering, where process gas flow rates must be adjusted to produce stoichiometrically correct films. AES analysis is performed on films deposited onto conductive substrates; silicon wafers are frequently used. XRD provides information about the crystal structure of the film. Improved crystal structure typically improves the electron transport in films, which should increase the light emission. XRD provides qualitative results about crystallinity, which may be correlated with light emission. XRD measurements are taken on films deposited on glass or quartz substrates. Aging studies provide information about the stability of films over time. Threshold voltages and B-V curves may shift positively or negatively over time, adversely affecting ACTFEL device performance. Certain fabrication and processing techniques can reduce these shifts, and aging studies can provide insight into how to produce more stable ACTFEL devices.

# CHAPTER 4 - EXPERIMENTAL RESULTS AND DISCUSSION

This chapter presents experiment results and a discussion of these results. Two targets are evaluated for sputtering thin-films for use as ACTFEL phosphors. Results obtained from different recipes for each target are given, along with characterization results of full ACTFEL devices. Also presented are the results of annealing under different conditions, the effects of variations of the process gas flow rates on physical measurements, and the effect of depositions at elevated temperatures on measured parameters and full ACTFEL devices.

## 4.1 The $Al_{0.8}In_{0.2}$:$Eu_2O_3$ (1 mole %) Target

### 4.1.1 Target Composition

The first target pressed to evaluate AlInN as an ACTFEL phosphor consists of 0.8 mole fraction aluminum and 0.2 mole fraction indium doped with 1 mole % europium in the form of $Eu_2O_3$. The composition of this target (referred to hereafter as the 0.8-0.2 target) is based on work by Kubota *et al.* [19] who reports the optical bandgap of AlInN versus the mole fraction of AlN. These data are presented below in Fig. 4-1. ZnS has an $E_{opt}$ of 3.75 eV [20], so an optical bandgap of around 3 eV for the 0.8-0.2 composition, as indicated in Fig. 4-1, is a reasonable starting point. Elemental powders are used as sources of aluminum and indium in the target since AlN and InN are expensive, and there is some doubt as to whether these nitrides would press into targets. $Eu_2O_3$ is used as the luminescent impurity because Eu has an ionic radius similar to that of indium, the same valence as the host lattice cation, and red luminescence is desired. The target's component masses, molar composition, and mole percent composition are given in Table 4-1.

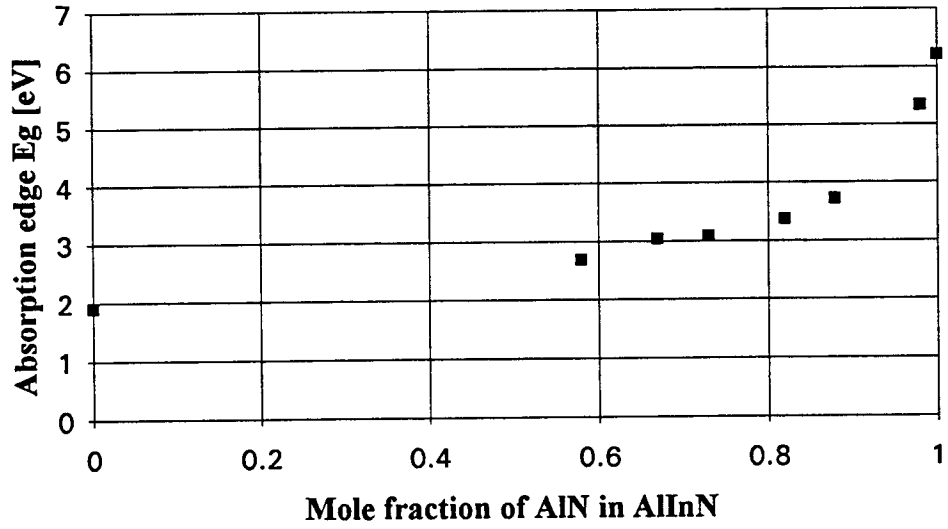


Figure 4-1. The optical bandgap of AlInN versus the mole fraction of AlN in AlInN (from Kubota *et al.* [19]).

Table 4-1 The $Al_{0.8}In_{0.2}$:$Eu_2O_3$ Target Composition

| Component | Mass | Moles | Mole % |
|---|---|---|---|
| Aluminum | 5.9500 g | 0.220500 | 79.3 |
| Indium | 6.2995 g | 0.054860 | 19.7 |
| Europium (as $Eu_2O_3$) | 0.4774 g | 0.002713 | 1.0 |

### 4.1.2 The 90/10/0 Recipe

The first recipe used to evaluate the 0.8-0.2 target is 90 standard cubic centimeters per minute (sccm) argon and 10 sccm nitrogen. (Recipes will be referred to hereafter as x/y/z, where x is the flow rate of argon, y is the flow rate of nitrogen, and z is the flow rate of the dilute nitrous oxide mixture, all expressed in sccm.) Kubota *et al.* [19] give approximate flow percents for depositing AlInN but the 90/10/0 values used are those

previously used by Nguyen [7]. Nguyen used a ZnMnSiN target, however, and did not require that all the nitrogen incorporated in his film be supplied by the process gas flows.

As for the remaining deposition parameters, the deposition power used is also from Nguyen [7], 70 W or 8.8 W/cm^2. The deposition pressure is set to approximately 20 mT. Several screening runs were performed to determine a relative maximum for the deposition rate; the results closely matched those of Kubota *et al.* [19]. The substrate heater is not used initially, but is evaluated later in Section 4.2.6.

Using the flow chart presented in Section 3.4, the target is evaluated. After the deposition parameters are set, depositions are performed on silicon wafers until a reproducible refractive index is obtained. A silicon wafer with the thin-film deposited on it is annealed and the PL is evaluated. A longer deposition on a glass substrate is performed and the deposition rate evaluated. A deposition on a glass substrate is performed and the breakdown field, bulk resistivity, and dielectric constant are determined. A deposition on a quartz substrate is performed and the absorbance measured, and the optical bandgap is determined. The recipe specifications and the physical, electrical, and optical parameters measured are given in Table 4-2. The bulk resistivity for this recipe is determined from an average from dots which exceeded a 1.0 MV/cm breakdown field.

Table 4-2 The 0.8-0.2 Target 90/10/0 Recipe and Measured Parameters

| | | | |
|---|---|---|---|
| Target = | $Al_{0.8}In_{0.2}$:$Eu_2O_3$ | Dep Rate = | 76 Å/min |
| Ar = | 90 sccm | $n$ = | 2.24 |
| $N_2$ = | 10 sccm | $\varepsilon_p$ = | 9.6 |
| $N_2O$ = | 0 sccm | $\rho$ = | $1.2 \times 10^{10}$ Ω*cm |
| Dep. Pres. = | 20 mT | $F_{br}$ = | 0.9 MV/cm |
| Dep. Power = | 70 W | $E_{opt}$ = | 2.15eV |
| | | PL = | dim red |

The refractive index is a useful monitor of run-to-run reproducibility and provides an indication of the film composition, but it is not an accurate measure of the actual composition of the film. Since the target is a metallic compound, the deposited system is at best a binary (AlN and InN) and more likely a quaternary ($Al_2O_3$, AlN, $In_2O_3$, and InN) mixture. An accurate estimation of the film's composition cannot be made from the refractive index due the problems associated with interpolating between the four constituent's refractive indices.

A Tauc plot for the deposited thin film is given in Fig. 4-2. Note that the straight line fit is good from ~ 3 - 4.5 eV, and shows evidence of band-tail states at the lower energies below about 2.5 eV. Note also the 2.15 eV optical bandgap is significantly less than that reported by Kubota *et al.* [19], i.e. ~ 3.3 eV.

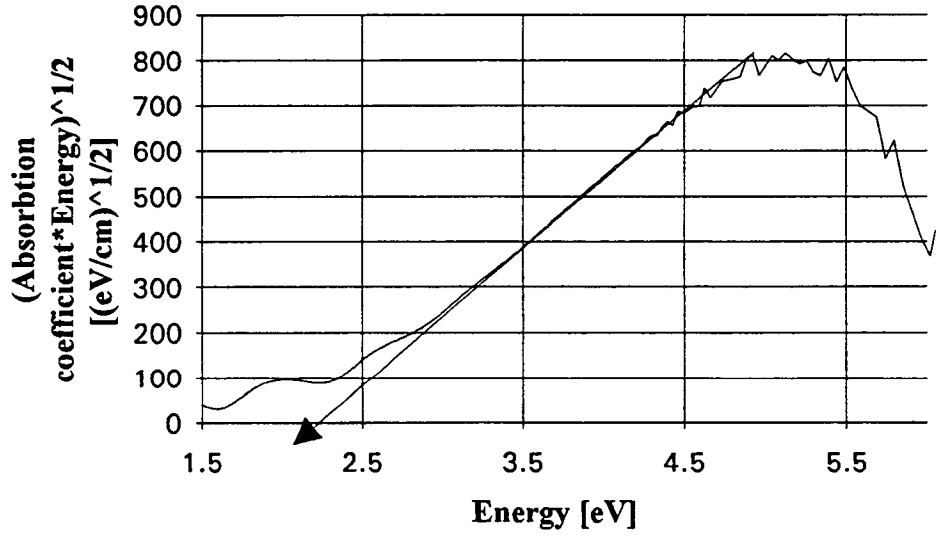


Figure 4-2. A Tauc plot for the 0.8-0.2 target 90/10/0 recipe film.

The photoluminescence of deposited thin films shows a dim red. The thin-films deposited onto silicon wafers are annealed at temperatures from 500 C to 800 C. The

thin-films show increasing brightness with higher temperature and a significant increase in PL between 600 C and 700 C. Wafers that are not annealed do not show PL. The steady increase in PL suggests that improving the film's crystallinity through higher-temperature annealing increases the PL, and that the film has a recrystallization temperature between 600 C and 700 C.

A deposition is performed on a DZA substrate to fabricate a full ACTFEL device. A $Q_i$-$V_a$ plot for the 90/10/0 recipe film, furnace annealed at 500 C for one hour, is shown in Fig 4-3. $C_i$ and $C_t$ can be determined using this plot, and $C_p$ is found by assuming that the insulator and phosphor layers are discrete capacitors in series. (A C-V plot generated for this device did not give conclusive values for $C_i$ and $C_t$. All subsequent $Q_{int}$-$F_p$ plots use $C_i$ and $C_t$ values determined from a $Q_i$-$V_a$ plot for that film, and $C_p$ is calculated from $C_i$ and $C_t$.) A $Q_{int}$-$F_p$ plot for the 90/10/0 recipe film is shown in Fig. 4-4. This device exhibits a significant amount of conduction charge, comparable to ZnS [16]. This indicates that a significant number of electrons are transported across the film during each voltage pulse. However, this device also has a low phosphor field at which conduction occurs. Because the field is low, the electrons have insufficient energy to impact excite luminescent impurities. The device produces an extremely dim white light.

B-V and spectral analysis are performed on the 90/10/0 recipe ACTFEL device. A B-V plot for the 90/10/0 recipe ACTFEL device is shown in Fig. 4-5. The device does not exhibit a sharp turn-on voltage or a saturated light output. A brightness of ~ 0.007 fL is produced by the ACTFEL device, which is much too low for any useful application. (The background luminance is ~ 0.002 fL, which is subtracted from the plot's maximum brightness of ~ 0.009 fL to produce the brightness value given above.)

A spectral analysis for the 90/10/0 recipe ACTFEL device is given in Fig. 4-6. It shows the light produced by the ACTFEL device has three peaks at 405 nm, 545 nm, and 675 nm, which correspond to violet, green, and red light, respectively. The analysis also shows lower but non-negligible contributions across the entire visible spectrum. The

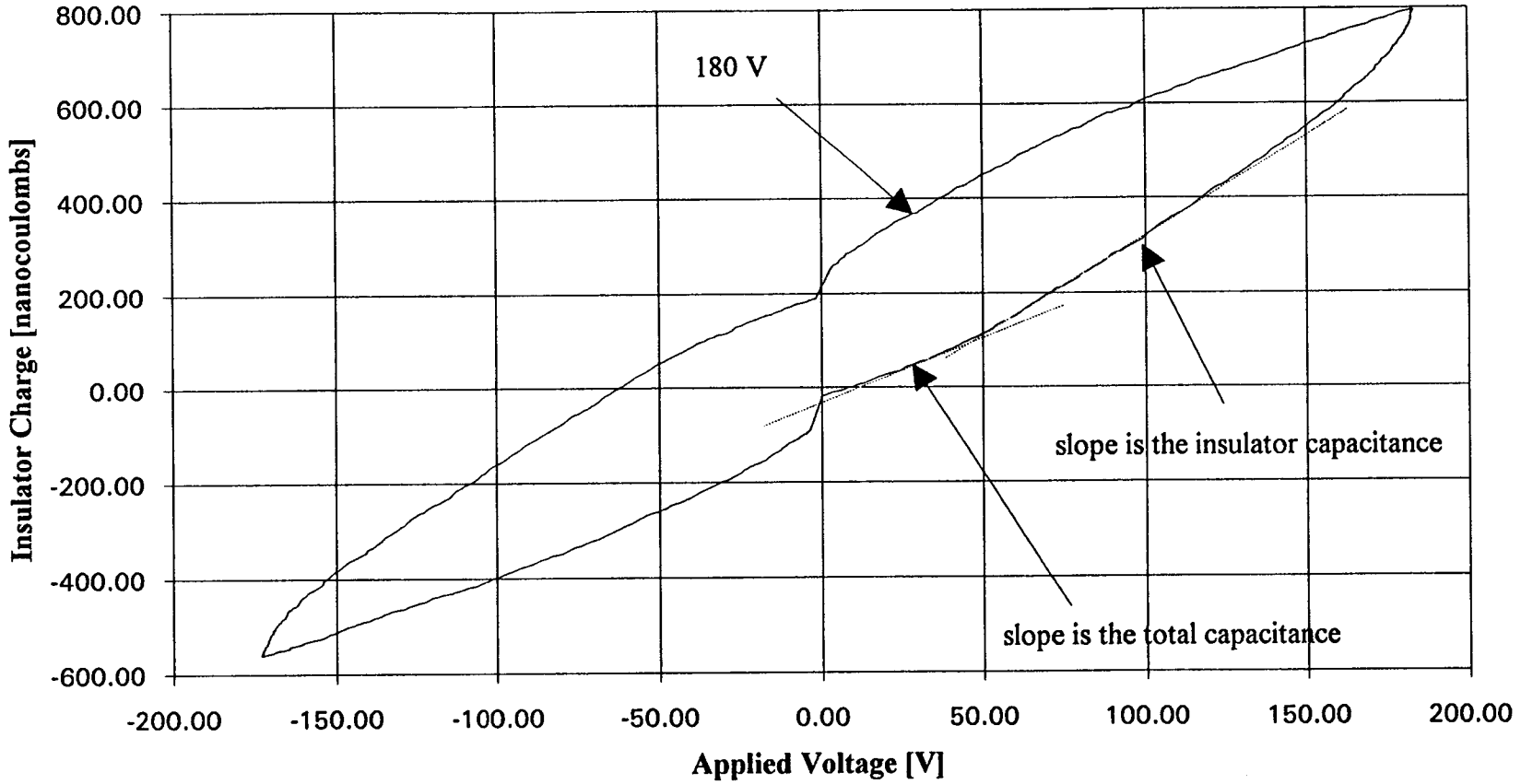


Figure 4-3. A $Q_i$-$V_a$ plot for the 0.8-0.2 target 90/10/0 recipe film.

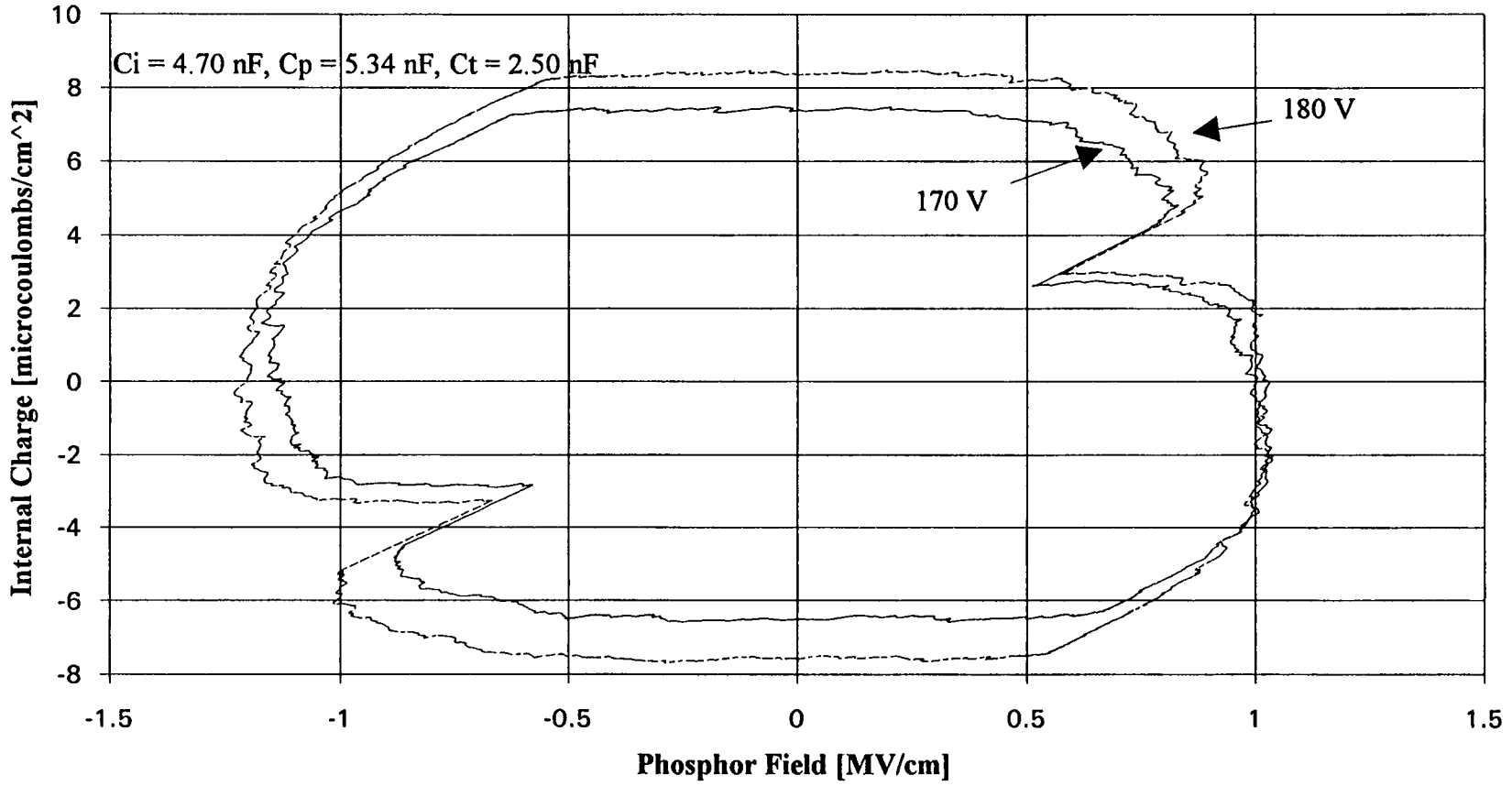


Figure 4-4. A $Q_{int}$-$F_p$ plot for the 0.8-0.2 target 90/10/0 recipe film.

analysis suggests that the light is produced by hot electron luminescence, where electrons in the conduction band radiatively recombine and produce photons of varying energies, rather that impact excitation, where electrons in excited states associated with the luminescent impurity radiatively relax and produce photons with energies (and light colors) characteristic of the luminescent impurity. The spectral analysis measurement was taken at 190 V.

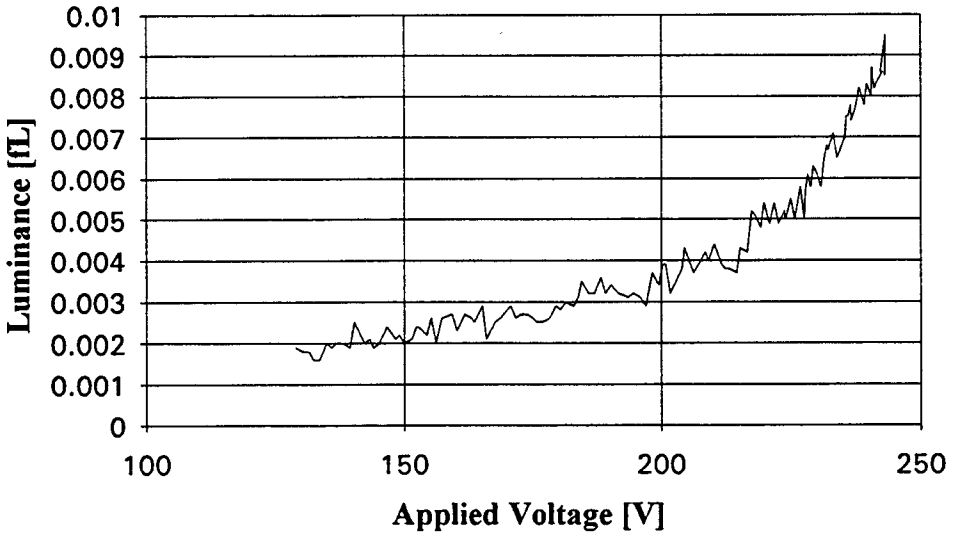


Figure 4-5. A B-V plot for the 0.8-0.2 target 90/10/0 recipe film.

Different anneals may be evaluated by fabricating a series of ACTFEL devices subjected to different annealing treatments. Annealing over 500 C produced ACTFEL devices with no measurable insulator capacitance, which suggests that indium is diffusing into the ATO layer. Also, anneals were attempted with 90/10/0 films deposited onto ITO substrates but produced films with low resistance and low breakdown field. These observations suggest that diffusion of indium into other layers occurs. As a result,

subsequent depositions onto ITO substrates are not annealed. The validity of this decision is evaluated in Section 4.2.5.

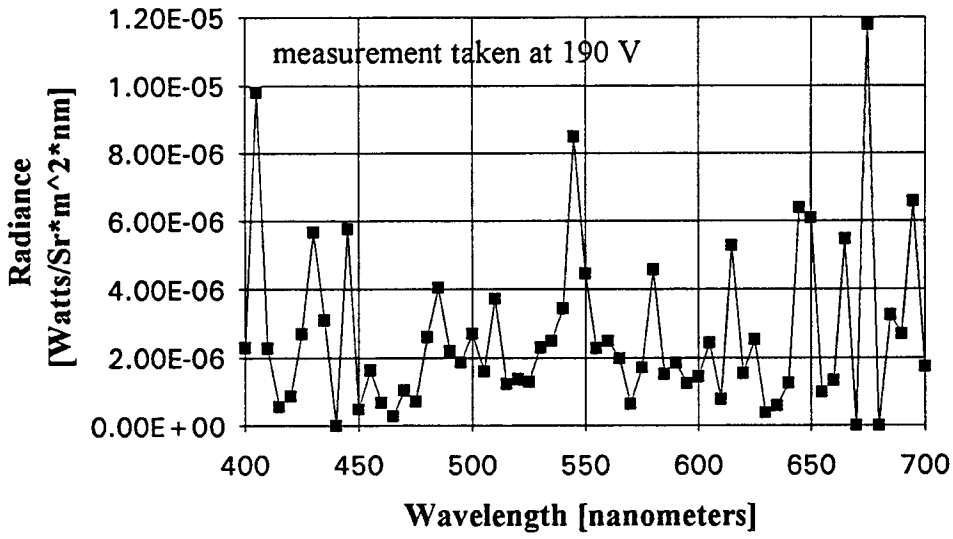


Figure 4-6. A spectral analysis of the 0.8-0.2 target 90/10/0 recipe film.

Because of the low phosphor field and $E_{opt}$, the next goal in optimizing the phosphor thin film using the 0.8-0.2 target is to increase the breakdown field and optical bandgap of the material slightly by introducing some $N_2O$ into the process gas flow. Oxides have larger bandgaps than nitrides and it was hoped that the introduction of $N_2O$ might change the deposited film enough to increase the clamping field and optical bandgap.

### 4.1.3 The 90/10/2 Recipe

The next recipe evaluated is 90/10/2. Only the gas flows are adjusted; no changes are made to the deposition pressure, deposition power, or substrate temperature.

(Throughout this work, the gas flows are adjusted such that the deposition pressure remains approximately constant at 20 mT. The deposition power is left constant at 70 W) The recipe specifications and the physical, electrical, and optical parameters measured are given in Table 4-3.

Table 4-3 The 0.8-0.2 Target 90/10/2 Recipe and Measured Parameters

| | | | |
|---|---|---|---|
| Target = | $Al_{0.8}In_{0.2}:Eu_2O_3$ | Dep Rate = | 86 Å/min |
| Ar = | 90 sccm | $n$ = | 2.00 |
| $N_2$ = | 10 sccm | $\varepsilon_p$= | 9.9 |
| $N_2O$ = | 2 sccm | $\rho$ = | $6.3 \times 10^{10}$ Ω*cm |
| Dep. Pres. = | 20 mT | $F_{br}$ = | 2.1 MV/cm |
| Dep. Power = | 70 W | $E_{opt}$ = | 2.2 eV |
| | | PL = | dim red |

The introduction of $N_2O$ yielded an increase in the deposition rate, as a result of the oxygen's more reactive nature compared to nitrogen. The large decrease in $n$ suggests a significant change in the film's composition. This is seen also in the breakdown field which more than doubles. Only a slight increase is seen in the optical bandgap. The PL results for this film show trends and results similar to the 90/10/0 recipe film. An increase in PL is seen with increasing anneal temperature, and a significant increase is seen between 600 C and 700 C. The 90/10/2 recipe produces only slightly brighter PL compared to the 90/10/0 recipe.

A $Q_{int}$-$F_p$ plot for the 90/10/2 recipe film, furnace annealed at 500 C for one hour, is shown in Fig. 4-7. Compared to the 90/10/0 recipe film, there is an increase in the phosphor field (i.e. 1.8 MV/cm versus 1.0 MV/cm), while there is a decrease in the conduction charge (i.e. 5 $\mu C/cm^2$ versus 8 $\mu C/cm^2$). The device appears to clamp during both pulses of the voltage waveform. The device produces a dim white light.

The 90/10/0 and 90/10/2 recipes show that AlInN has promise as an ACTFEL phosphor. There is significant conduction charge and some light is emitted. The next step in the evaluation of this target is to deposit and evaluate a stoichiometrically correct $Al_{0.8}In_{0.2}N$ film.

### 4.1.4 Evaluation of the Refractive Index versus Gas Flow Rates

The refractive index can be used to monitor changes in thin-films as the composition of the deposited film changes from a metallic or nitrogen-deficient film to a stoichiometrically correct nitride. Eventually, the index should stabilize at a value for that of a thin-film with the maximum amount of nitrogen incorporated. This may not, however, be stoichiometrically correct.

An experiment is performed to evaluate the refractive index as a function of the percent of nitrogen in an argon-nitrogen process gas flow. The result is shown in Fig. 4-8. The deposition rate is also shown. Significant changes occur in the deposition rate, as a consequence of the lower concentration of Ar and, hence, a lower concentration of $Ar^+$ ions. These ions are responsible for ejecting the AlN or InN molecules from the target, so reducing their concentration will reduce the deposition rate. The plot shows that even at a nitrogen flow of nearly 50 %, the refractive index shows significant changes without having reached a limit.

Although the film index has not reached a limit, the film is evaluated to determine how these changes affect the electrical and optical properties.

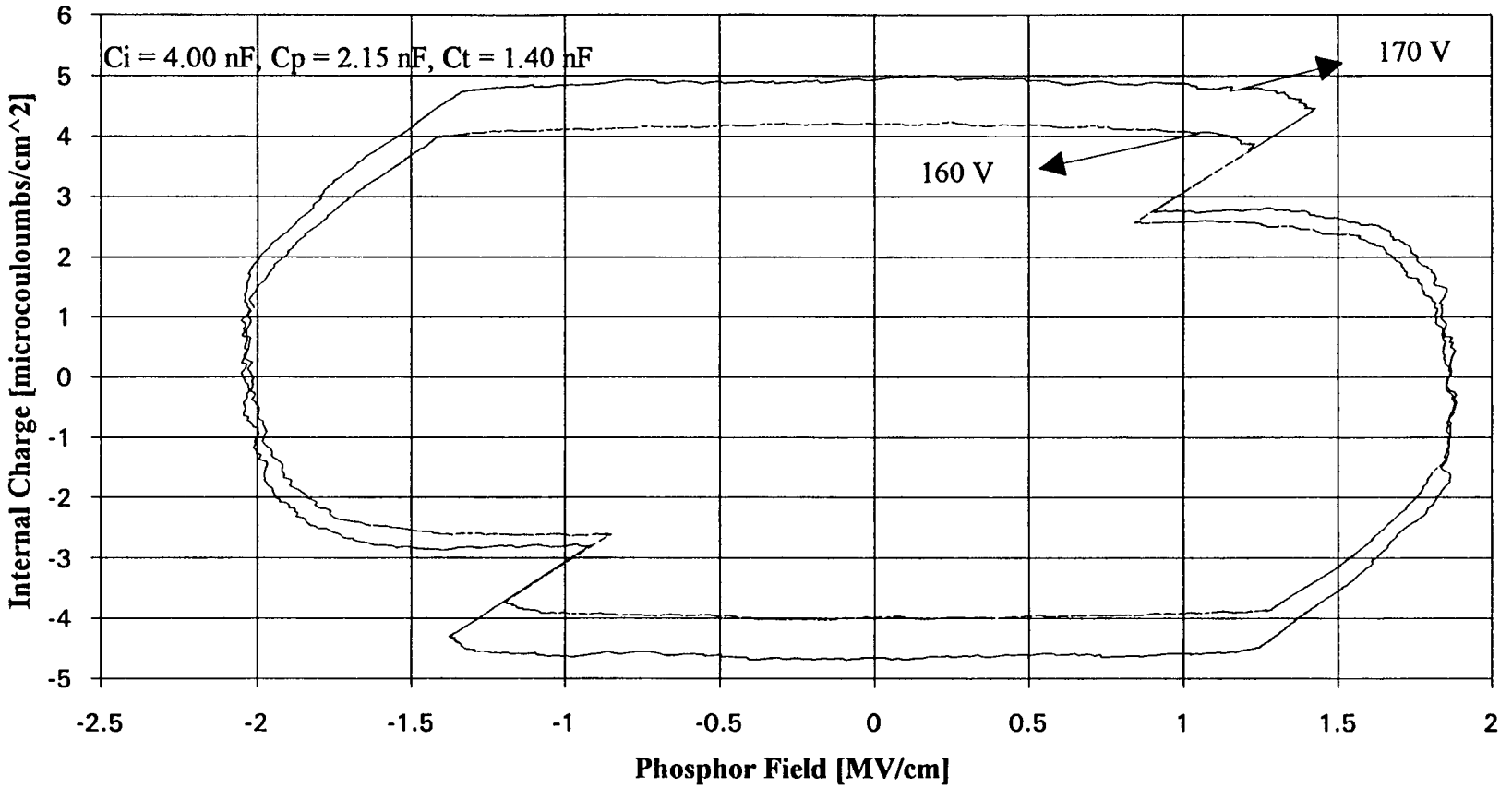


Figure 4-7. A $Q_{int}$-$F_p$ plot for the 0.8-0.2 target 90/10/2 recipe film.

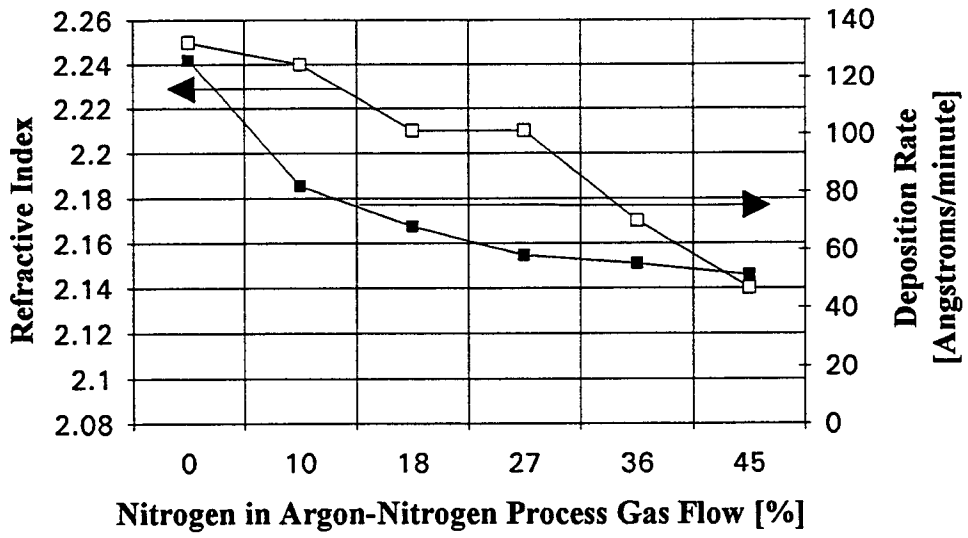


Figure 4-8. The refractive index and deposition rate of the deposited thin-film versus the % of nitrogen in the argon-nitrogen process gas flow.

### 4.1.5 The 60/50/0 Recipe

The next recipe evaluated is 60/50/0. The recipe specifications and the physical, electrical, and optical parameters measured are given in Table 4-4.

The deposition rate and refractive index are significantly lower than the 90/10/0 recipe film. The breakdown field is very low, approximately 0.2 MV/cm. Because of this, resistivity measurements are not possible at 1 MV/cm. Also, the dielectric constant exhibits a large degree of frequency dispersion, as indicated in Fig. 4-9, presumably associated with the leaky nature of the deposited thin-film. Figure 4-10 gives the Tauc plots for the 90/10/0 and 60/50/0 recipes. The optical bandgap is 2.0 eV, slightly lower than the 90/10/0 recipe.

Table 4-4 The 0.8-0.2 Target 60/50/0 Recipe and Measured Parameters

| | | | |
|---|---|---|---|
| Target = | $Al_{0.8}In_{0.2}:Eu_2O_3$ | Dep Rate = | 45 Å/min |
| Ar = | 60 sccm | $n$ = | 2.14 |
| $N_2$ = | 50 sccm | $\varepsilon_p$ = | na |
| $N_2O$ = | 0 sccm | $\rho$ = | na |
| Dep. Pres. = | 20 mT | $F_{br}$ = | 0.2 MV/cm |
| Dep. Power = | 70 W | $E_{opt}$ = | 2.0 eV |
| | | PL = | faint red |

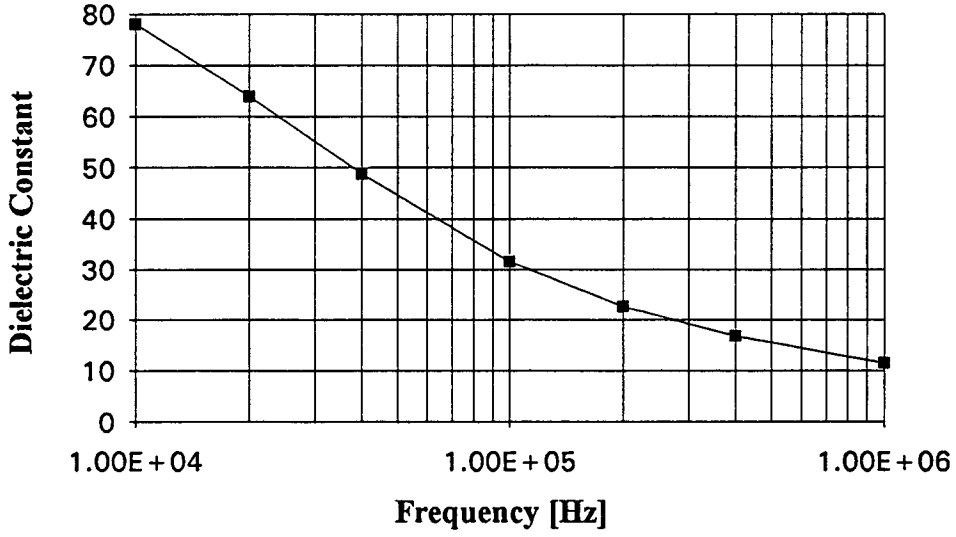


Figure 4-9. The dielectric constant of the 0.8-0.2 target 60/50/0 recipe film.

Figure 4-10 shows only a slight change in the bandgap as a function of recipe; the value of $E_{opt}$ is a weak function of the recipe used. The difference in the curves at energies above 4 eV is a result of the different absorbances of the substrates used. The 90/10/0 measurement is taken on quartz while the 60/50/0 measurement is on a glass substrate. Quartz has a flat absorption response for high energies while glass does not, which prevents accurate measurements at high energy ranges.

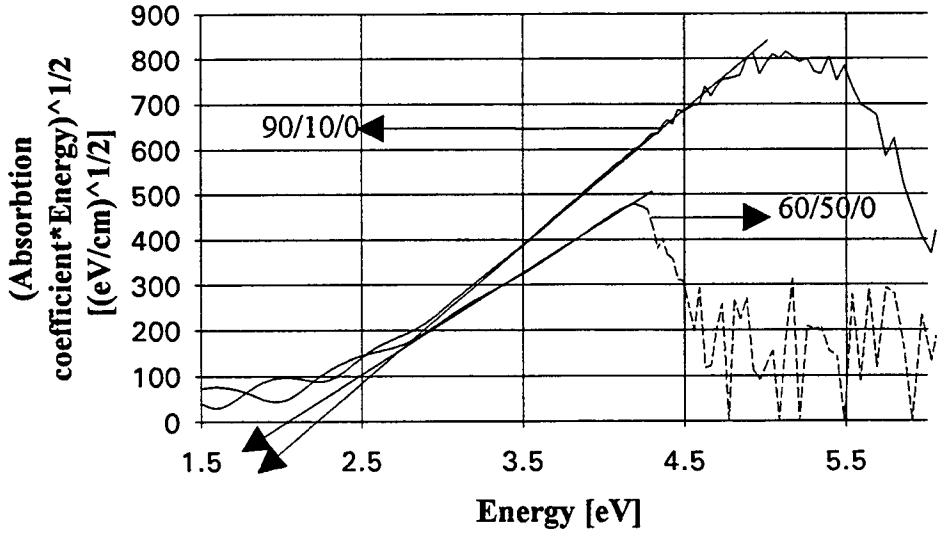


Figure 4-10. Tauc plots for the 0.8-0.2 target 90/10/0 and 60/50/0 recipe films.

The PL intensity of this recipe film is evaluated. Similar trends are seen in the recipe compared to previous recipes. The color produced is red, while the brightness is lower than that of the 90/10/0 recipe film.

In summary, a significant change occurs in the deposited thin-film as changes are made in the process gas flow. However, the measured parameters are not suitable for ACTFEL device phosphors. The breakdown field is too low, the PL intensity decreases, and the dielectric constant varies significantly over frequency. To continue evaluating AlInN as an ACTFEL phosphor, a new target is required. The new target needs a larger host lattice bandgap to increase the bulk resistivity and breakdown field of the phosphor. This is accomplished by increasing the mole fraction of aluminum because a larger Al concentration results in a larger bandgap.

## 4.2 The $Al_{0.9}In_{0.1}$:$EuF_3$ (1 mole %) Target

### 4.2.1 Target Composition

The second target used to evaluate AlInN as an ACTFEL phosphor consists of 0.9 mole fraction aluminum and 0.1 mole fraction indium doped with 1 mole % europium in the form $EuF_3$. The composition of this target (referred to hereafter as the 0.9-0.1 target) is based on results from the first target evaluated which indicate that a larger bandgap is required for the host lattice. The change in the luminescent impurity from $Eu_2O_3$ to $EuF_3$ is based on the results of Kido *et al.* [8] which show good luminescent intensities from rare earth elements bonded to halogens. Europium is used since red luminescence is desired. The target's component masses, molar composition, and mole percent composition are given in Table 4-5.

Table 4-5 The $Al_{0.9}In_{0.1}$:$EuF_3$ Target Composition

| Component | Mass | Moles | Mole % |
|---|---|---|---|
| Aluminum | 6.8182 g | 0.252700 | 89.1 |
| Indium | 3.2215 g | 0.028060 | 9.9 |
| Europium (as $EuF_3$) | 0.5936 g | 0.002841 | 1.0 |

### 4.2.2 The 60/50/0 Recipe

The first flow rate recipe used to evaluate the 0.9-0.1 target is 60/50/0. This starting point is used as the higher-argon-percentage recipes do not produce a stoichiometrically correct nitride. The recipe specifications and the physical, electrical, and optical parameters measured are given in Table 4-6.

Table 4-6 The 0.9-0.1 Target 60/50/0 Recipe and Measured Parameters

| | | | |
|---|---|---|---|
| Target = | $Al_{0.9}In_{0.1}:EuF_3$ | Dep Rate = | 43 Å/min |
| Ar = | 60 sccm | $n$ = | 1.97 |
| $N_2$ = | 50 sccm | $\varepsilon_p$ = | 11.4 |
| $N_2O$ = | 0 sccm | $\rho$ = | $4.1 \times 10^{11}$ Ω*cm |
| Dep. Pres. = | 20 mT | $F_{br}$ = | 3.0 MV/cm |
| Dep. Power = | 70 W | $E_{opt}$ = | 2.5 - 2.8 eV |
| | | PL = | dim red |

While the deposition rate and refractive index remain fairly constant with respect to the 0.9-0.1 target 60/50/0 recipe film, the breakdown field has increased significantly. A breakdown field of 3.0 MV/cm may be slightly high for an ACTFEL phosphor, but the trend displayed by the 0.8-0.2 target is a decreasing $F_{br}$ with increasing nitrogen content, which suggests that the 0.9-0.1 target can provide the proper breakdown field in a stoichiometrically correct AlInN. A Tauc plot is shown in Fig 4-11. The optical bandgap of 2.5 eV shown in Fig. 4-9 does not agree with the results given by Kubota *et al.* [19] in which the optical bandgap is ~ 4 eV. The deposited thin film shows PL, with trends, colors, and intensities similar to that of films deposited from the 0.8-0.2 target using the 60/50/0 recipe film.

The next step in evaluation is to deposit a stoichiometrically correct nitride and to evaluate it. A recipe with a significantly higher nitrogen concentration is selected for evaluation.

### 4.2.3 The 20/60/0 Recipe

The next recipe used to evaluate the 0.9-0.1 target is 20/60/0. Instead of running an experiment to determine the refractive index based on the nitrogen concentration of the process gas flow, a recipe with a significantly higher nitrogen concentration is used. The

gas flows selected are based on the results of Kubota *et al.* [19] who used 90 % nitrogen for AlN depositions and 50 % nitrogen for AlInN depositions. The recipe specifications and the physical, electrical, and optical parameters measured are given in Table 4-7. The breakdown field is reduced from 3.0 MV/cm to 2.3 MV/cm in going from the 60/50/0 recipe to the 20/60/0 recipe while only minor changes result in other parameters.

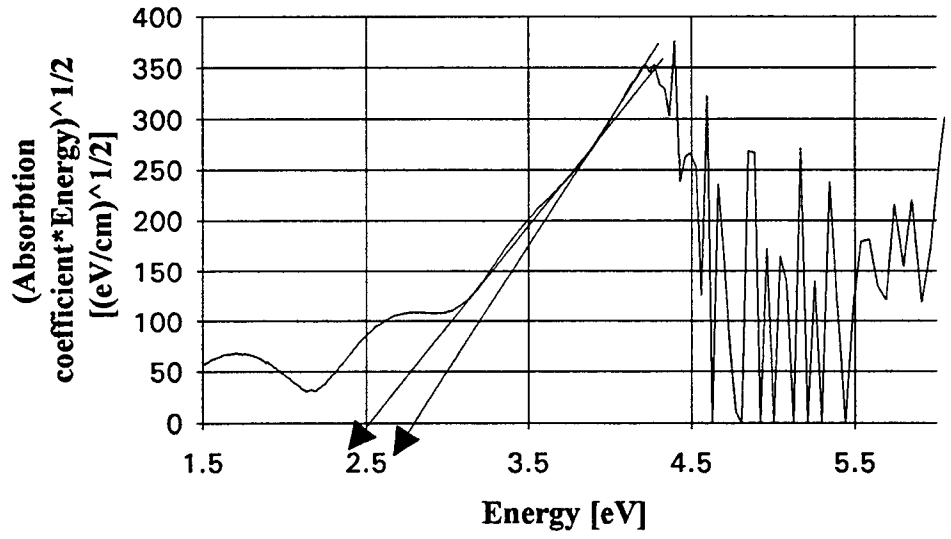


Figure 4-11. A Tauc plot for the 0.9-0.1 target 60/50/0 recipe film.

Table 4-7 The 0.9-0.1 Target 20/60/0 Recipe and Measured Parameters

| | |
|---|---|
| Target = $Al_{0.9}In_{0.1}:EuF_3$ | Dep Rate = 35 Å/min |
| Ar = 20 sccm | $n$ = 2.00 |
| $N_2$ = 60 sccm | $\varepsilon_p$ = 10.8 |
| $N_2O$ = 0 sccm | $\rho = 1.0 \times 10^{10}$ Ω*cm |
| Dep. Pres. = 20 mT | $F_{br}$ = 2.3 MV/cm |
| Dep. Power = 70 W | $E_{opt}$ = 2.3 - 2.7 eV |
| | PL = dim red |

AES analysis is performed on the 20/60/0 deposited thin film. The results are given in Table 4-8. The Eu concentration was below the AES detection limit (~ 1 %). Because no oxygen (as either $O_2$ or $N_2O$) is intentionally added to the process gas flows or incorporated into the target, the large O content indicates that a significant atmospheric leak is present in the system. After the system was He leak-checked, a leak was identified in the process gas manifold and repaired. AES analysis is performed on the film deposited in the repaired system, and the results are given in Table 4-9. A definite reduction is made in the oxygen incorporation in the deposited thin-film but it is not completely eliminated.

Table 4-8 AES Analysis of the 0.9-0.1 Target 20/60/0 Recipe Film

| Element | Target Composition (mole %) | Film Composition (mole %) |
|---|---|---|
| Aluminum | 89.1 | 47 |
| Indium | 9.9 | 3 |
| Europium | 1.0 | - |
| Nitrogen | - | 32 |
| Oxygen | - | 18 |

Table 4-9 AES Analysis of the 0.9-0.1 Target 20/60/0 Recipe Film (after leak is fixed)

| Element | Target Composition (mole %) | Film Composition (mole %) |
|---|---|---|
| Aluminum | 89.1 | 44 |
| Indium | 9.9 | 2 |
| Europium | 1.0 | - |
| Nitrogen | - | 42 |
| Oxygen | - | 7 |
| Carbon | - | 5 |

The recipe is re-characterized after the leak was fixed; the recipe specifications and the physical, electrical, and optical parameters measured are given in Table 4-10. The

refractive index increases from 2.00 to 2.04. This shift is consistent with the formation of a better nitride which typically has a larger $n$ than the corresponding oxide. A significant increase occurs in the dielectric constant upon fixing the leak; this is also consistent with a thin-film composition which is closer to a nitride than an oxide. An increase is seen in PL for the 20/60/0 recipe after the leak is fixed, producing red luminescence with a brightness comparable to the 0.8-0.2 target 90/10/0 recipe film.

Table 4-10 The 0.9-0.1 Target 20/60/0 Recipe and Measured Parameters (after leak is fixed)

| | | | |
|---|---|---|---|
| Target = | $Al_{0.9}In_{0.1}:EuF_3$ | Dep Rate = | 35 Å/min |
| Ar = | 20 sccm | $n$ = | 2.04 |
| $N_2$ = | 60 sccm | $\varepsilon_p$ = | 12.9 |
| $N_2O$ = | 0 sccm | $\rho$ = | $5.5 \times 10^{10}$ Ω*cm |
| Dep. Pres. = | 20 mT | $F_{br}$ = | 2.3 MV/cm |
| Dep. Power = | 70 W | $E_{opt}$ = | 2.7 eV |
| | | PL = | dim red |

A deposition is done on a DZA substrate and the film is RTP annealed at 500 C for 2 minutes. A $Q_{int}$-$F_p$ plot for the 20/60/0 recipe film after the leak is fixed is given in Fig 4-12. There is significantly less conduction charge (i.e. 0.5 $\mu C/cm^2$ compared to 5 $\mu C/cm^2$ for the 90/10/2 recipe film) than observed for previously deposited thin films and a small steady-state field (i.e. 1.0 MV/cm compared to 1.7 MV/cm for the 90/10/2 recipe film). An extremely dim white light is produced by this ACTFEL device.

Higher-temperature anneals are evaluated for the 20/60/0 recipe as follows. A $Q_{int}$-$F_p$ plot for a 20/60/0 recipe thin film, annealed at 650 C for 10 seconds, is given in Fig. 4-12. While the conduction charge increases with annealing (i.e. 1.0 $\mu C/cm^2$ versus 0.5 $\mu C/cm^2$), it is significantly lower than that obtained for previous films. The phosphor field also increases slightly with annealing (i.e. 1.2 MV/cm versus 1.0 MV/cm), but since

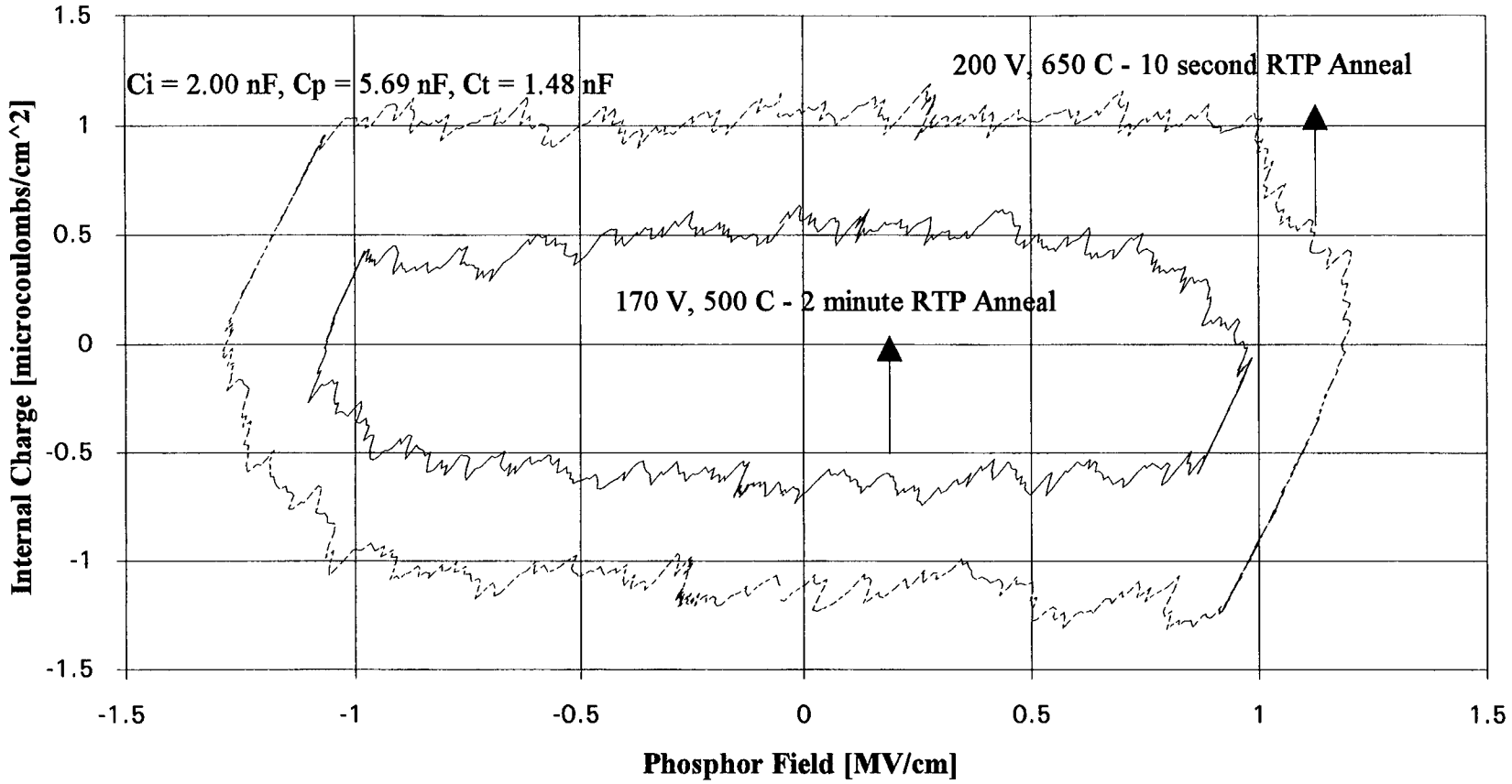


Figure 4-12. $Q_{int}$-$F_p$ plots for the 0.9-0.1 target 20/60/0 recipe film with different annealing conditions.

different maximum voltages are used in the two curves, a direct comparison is not possible for the data shown in Fig. 4-12. The white light emission from the ACTFEL device is extremely dim. Deposition of a 20/60/0 thin film is accomplished using a DZA substrate and is RTP annealed at 750 C for 10 seconds; unfortunately, this high an annealing temperature led to delamination problems and so it was not pursued any further.

The next step in evaluating AlInN is to press a new target with a larger bandgap, (i.e. a larger mole fraction of aluminum to increase the phosphor field and $F_{br}$). However, AES analysis shows that the system cannot produce an oxygen-free AlInN film. Until such a film can be deposited, it is not possible to evaluate AlInN further as an ACTFEL phosphor. The time frame for the work required to completely eliminate oxygen from the system cannot be accomodated within the work presented in this thesis. Therefore, evaluation of AlInN as an ACTFEL phosphor did not continue.

There are certain adjustments, however, that can be used to engineer a material deposited from this target to produce a more efficient ACTFEL phosphor. The next step in developing a phosphor is the addition of $N_2O$ to the process gas flow, which is known to increase phosphor field and luminescence.

### 4.2.4 The 20/55/3 Recipe

The next recipe used is 20/55/3. Once run-to-run reproducibility is established, evaluation of the deposited thin-film is accomplished using a full ACTFEL device. The goal of this set of runs is to see the effects of adding $N_2O$ to the process gas flow on the conduction charge and clamping field. Evaluation of the film on an ITO substrate is unnecessary since $\varepsilon_p$ is not required to produce the $Q_{int}$-$F_p$ plot.

A $Q_{int}$-$F_p$ plot for the 20/55/3 recipe, RTP annealed at 650 C for 10 seconds, is given in Fig. 4-13. There is a significant increase in the conduction charge (i.e. 4 $\mu C/cm^2$

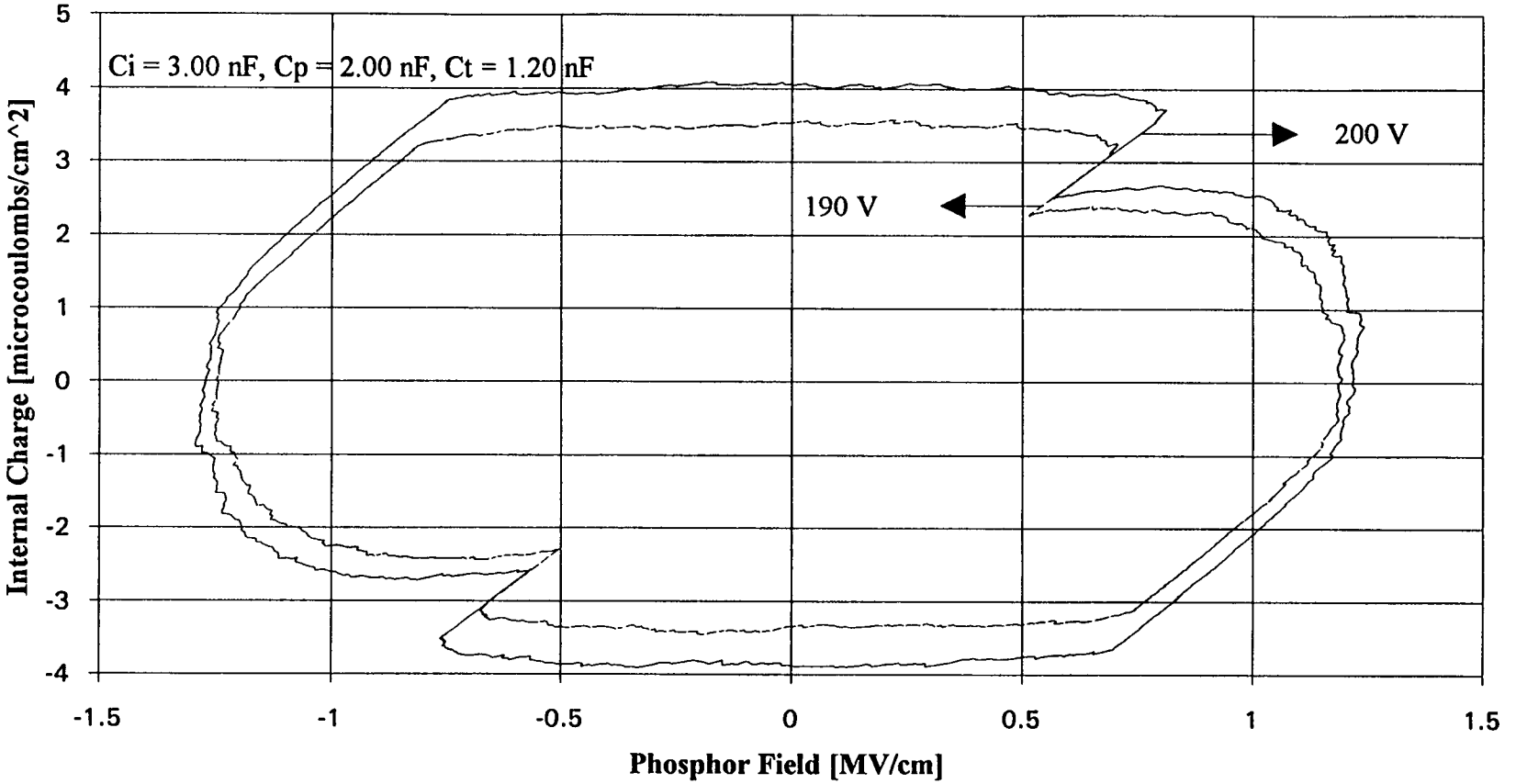


Figure 4-13. A $Q_{int}$-$F_p$ plot for the 0.9-0.1 target 20/55/3 recipe film.

versus 1 $\mu C/cm^2$). A slight increase is seen in white light emission from the device compared to the 20/60/0 recipe ACTFEL device.

Based on the increases observed in the conduction charge and phosphor field, the next development step is to increase the $N_2O$ flow rate to further increase these measured values.

### 4.2.5 The 20/50/8 Recipe

The next recipe used is 20/50/8. Like the 20/55/3 evaluation, a deposition is performed on a DZA substrate after establishing run-to-run reproducibility to evaluate the conduction charge and phosphor field.

A $Q_{int}$-$F_p$ plot for the 20/50/8 recipe, RTP annealed at 650 C for 10 seconds, is given in Fig. 4-14. There is a slight decrease in the conduction charge (i.e. 3 $\mu C/cm^2$ versus 4 $\mu C/cm^2$) and a slight increase in the phosphor field (i.e. 1.4 MV/cm versus 1.2 MV/cm). The device emits a dim white light, comparable to the 20/55/3 recipe ACTFEL device.

Two different depositions are performed on an ITO substrate to evaluate the effect of annealing on the electrical parameters measured. The recipe specifications and the physical, electrical, and optical parameters measured are given in Table 4-11. The parameters in parentheses are for the annealed film. An RTP anneal of 650 C for 10 seconds is used.

Only slight changes are produced in the dielectric constant while the breakdown field is nearly halved. The annealed film's $F_{br}$ agrees closely with the steady-state phosphor field; this agreement between $F_{br}$ and the phosphor field measured via a $Q_{int}$-$F_p$ plot is not observed for all of the previous samples analyzed. The bulk resistivity also decreases with annealing. Tauc plots for the two deposited thin-films before and after annealing are given in Fig. 4-15. The optical bandgap is unchanged with annealing.

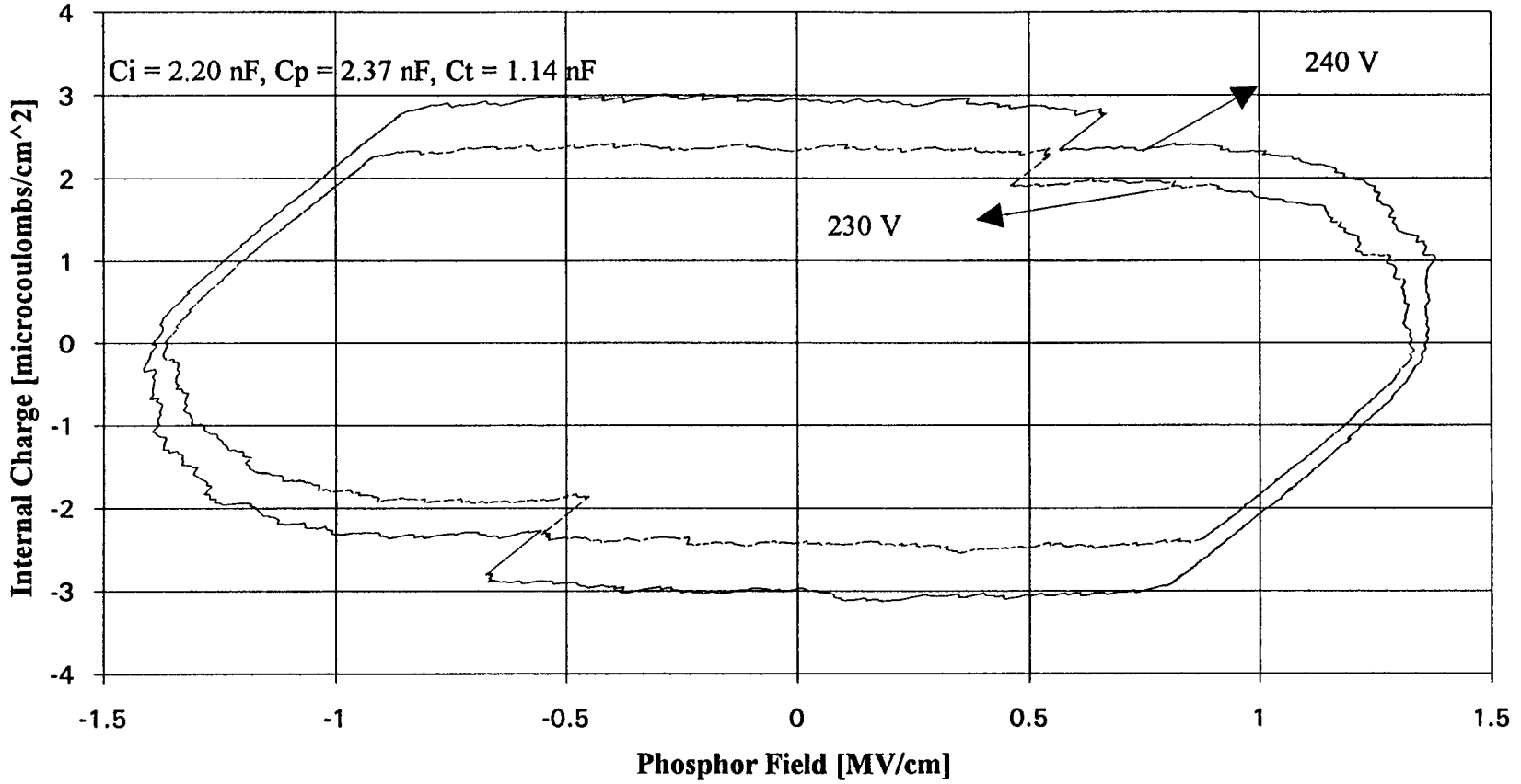


Figure 4-14. A $Q_{int}$-$F_p$ plot for the 0.9-0.1 target 20/50/8 recipe film.

Table 4-11 The 0.9-0.1 Target 20/50/8 Recipe and Measured Parameters

| | | | |
|---|---|---|---|
| Target = | $Al_{0.9}In_{0.1}:EuF_3$ | Dep Rate = | 39 Å/min |
| Ar = | 20 sccm | $n$ = | 1.61 |
| $N_2$ = | 50 sccm | $\varepsilon_p$ = | 11.1 (11.2) |
| $N_2O$ = | 8 sccm | $\rho$ = | 2.3 x $10^{10}$ Ω*cm (2.4 x $10^9$) |
| Dep. Pres. = | 20 mT | $F_{br}$ = | 2.7 (1.5) MV/cm |
| Dep. Power = | 70 W | $E_{opt}$ = | 2.4 eV |
| | | PL = | dim red |

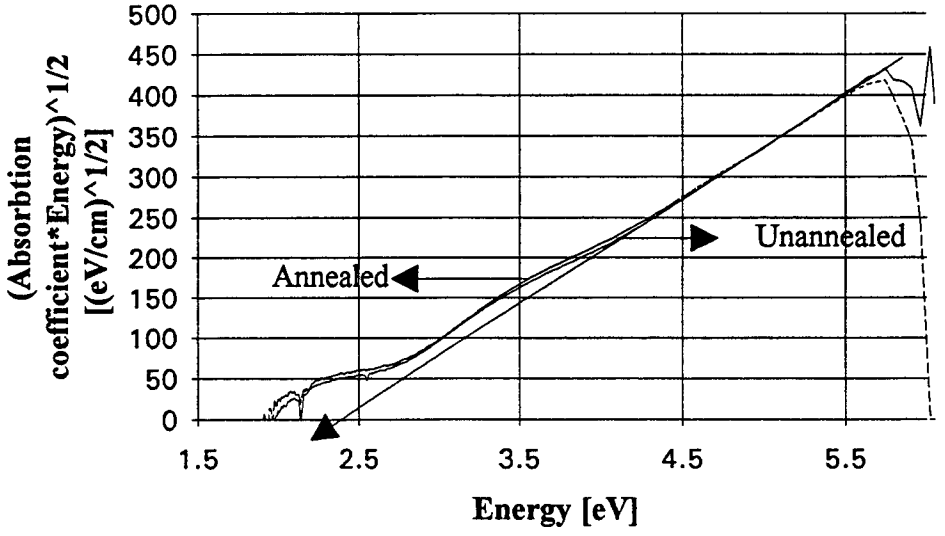


Figure 4-15. Tauc plots for the 0.9-0.1 target 20/50/8 recipe film before and after annealing.

Annealing thin-films deposited onto ITO substrates either makes little change in the measured parameters, such as the case for $\varepsilon_p$, or produces values in closer agreement with results from other evaluation techniques, such as $F_{br}$ and the steady-state phosphor field $F_{ss}$ from a $Q_{int}$-$F_p$ plot.

The PL intensity is evaluated on the 20/50/8 recipe film. Minor changes are seen in the brightness and color produced compared to the 20/60/0 recipe film. The film is slightly brighter than the 20/60/0 recipe film and the color is a darker red.

AES analysis is performed on the 20/50/8 recipe film. The results are given in Table 4-12. The film contains approximately 16 % nitrogen and approximately 27 % oxygen. Aluminum and indium still make up approximately 50 % of the film, as expected.

Table 4-12 AES Analysis of the 0.9-0.1 Target 20/50/8 Recipe Film

| Element | Target Composition (mole %) | Film Composition (mole %) |
|---|---|---|
| Aluminum | 89.1 | 49 |
| Indium | 9.9 | 1 |
| Europium | 1.0 | - |
| Nitrogen | - | 16 |
| Oxygen | - | 27 |
| Carbon | - | 7 |

Although increases are made in the steady-state phosphor field with some decrease in the conduction charge, it is unlikely that significant changes could be made in these parameters. The change in magnitude of the steady-state phosphor field drops steadily as the film's recipe changes from 20/60/0 to 20/55/3 to 20/50/8. AES analysis shows the deposited thin film is mostly an oxide using the 20/50/8 recipe. Greater additions of $N_2O$ probably will not increase the steady-state phosphor field beyond 1.5 MV/cm and may reduce the conduction charge even further. For this reason, no further increases in $N_2O$ were evaluated. The next step in the evaluation is the effect of increasing the substrate temperature during film deposition.

### 4.2.6 20/50/8 Recipe Films Deposited at Elevated Temperatures

The results of Kubota *et al.* [19] are for AlInN films deposited at 500 C. (No deposition conditions are reported by Kido *et al.* [8].) The substrate heater cannot produce 500 C so a deposition temperature of approximately 200 C is evaluated. The $Q_a$-$V_a$ and $Q_{int}$-$F_p$ plots for the 20/50/8 recipe film, deposited on a DZA substrate at ~ 200 C using the substrate heater and subsequently RTP annealed at 650 C for 10 seconds, are given in Figs. 4-16 and 4-17, respectively.

The $Q_i$-$V_a$ plot is given to show the significant increase in the insulator charge for the heated-substrate-deposited ACTFEL device (referred to hereafter as the heated device) compared to the unheated-substrate-deposited ACTFEL device (referred to hereafter as the unheated device) using the 20/50/8 process recipe. The heated device has a maximum insulator charge of ~ 1400 nC compared to ~ 360 nC for the unheated device. (The $Q_i$-$V_a$ plot for the unheated device is not shown.) The heated device also burns out (catastrophic breakdown) at 110 V compared to 240 V for the unheated device.

The $Q_{int}$-$F_p$ plot is shown using the $C_i$ and $C_t$ values obtained from the $Q_i$-$V_a$ plot. The shape of the $Q_{int}$-$F_p$ plot is highly dependent on the values of $C_i$ and $C_t$ used, and the values obtained from Fig. 4-16 are significantly larger than those obtained via the same method for the unheated device (i.e. 12.5 nF and 6.25 nF versus 2.20 nF and 1.14 nF). The $C_i$ and $C_t$ used to generate the plot can be adjusted to produce a plot with rectangular shape but those values for $C_i$ and $C_t$ are even larger than those obtained from Fig. 4-16. The $Q_{int}$-$F_p$ plot is difficult to interpret but the maximum internal charge increases significantly compared to the unheated device (i.e. 25 $\mu C/cm^2$ versus 3 $\mu C/cm^2$) while the maximum phosphor field is reduced (i.e. 1.0 MV/cm versus 1.4 MV/cm).

The effect of deposition temperature on the optical bandgap is evaluated. A thin-film is deposited onto a quartz substrate at 200 C and absorbance of the film is measured. No RTP anneal is performed following the deposition. Figure 4-18 shows the 20/50/8

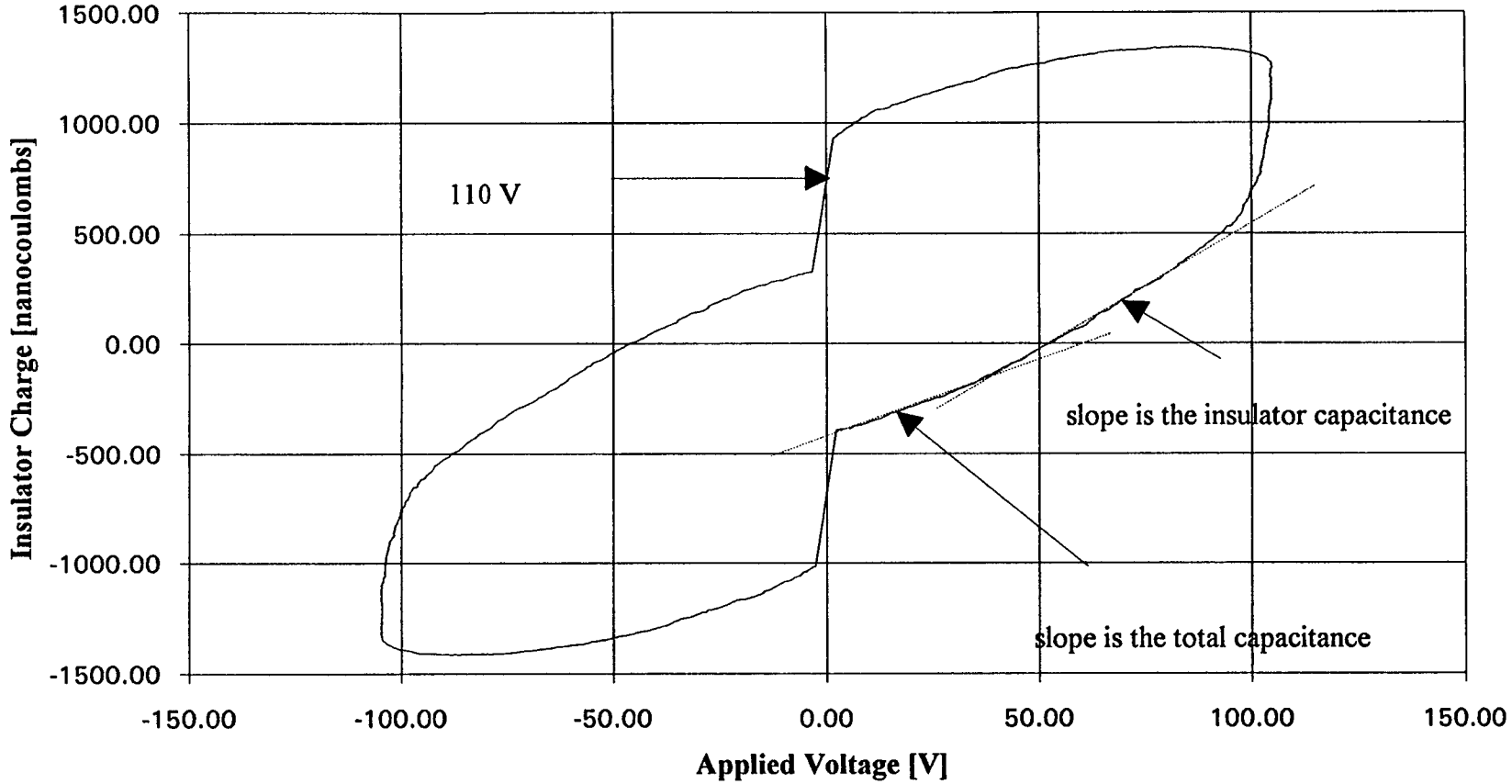


Figure 4-16. A $Q_i$-$V_a$ plot for the 0.9-0.1 target 20/50/8 recipe film deposited at 200 C.

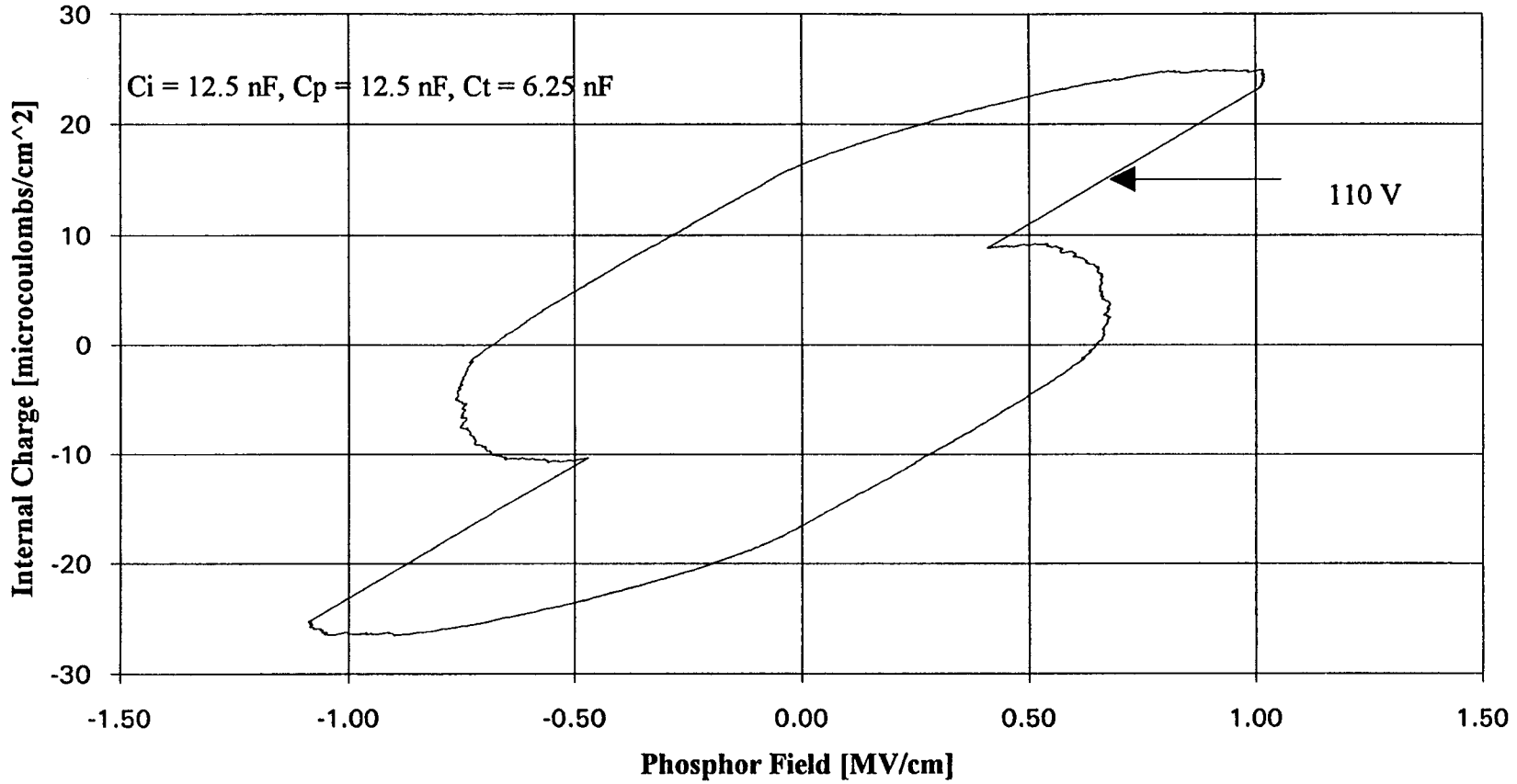


Figure 4-17. A $Q_{int}$-$F_p$ plot for the 0.9-0.1 target 20/50/8 recipe film deposited at 200 C.

recipe film annealed at 650 C for 10 seconds (without substrate heating during deposition) and deposited onto a heated quartz substrate at 200 C (without a subsequent RTP anneal). The optical bandgap for the heated deposition decreases compared to the RTP annealed film (i.e. 1.3 eV versus 2.4 eV). The effect of deposition temperature is analyzed using XRD. The quartz samples described above are analyzed and no evidence for crystallinity is found for either sample.

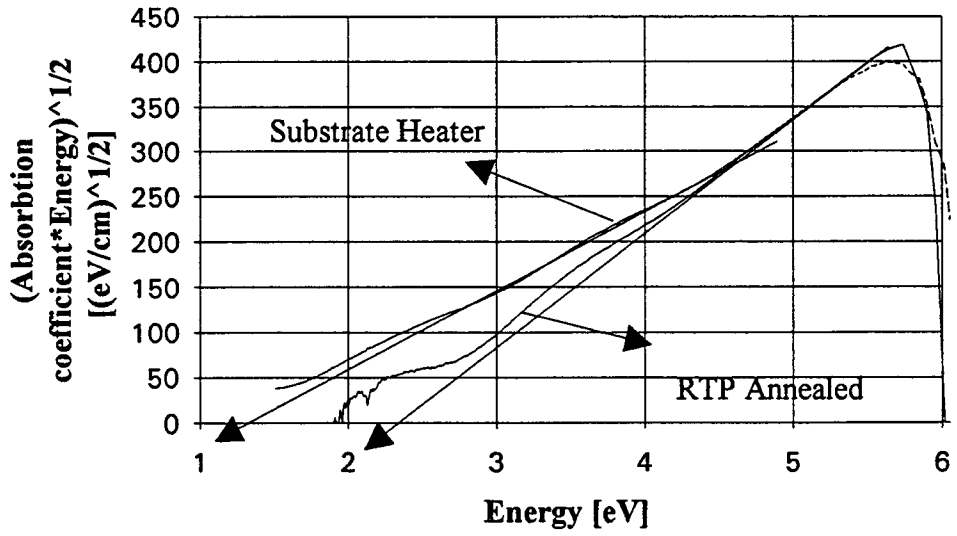


Figure 4-18. Tauc plots for the 0.9-0.1 target 20/50/8 recipe film deposited using the substrate heater and with an RTP anneal.

Heating the substrate significantly effects the deposited thin-film's optical bandgap, the ACTFEL device's conduction charge, the maximum phosphor field, and the burn-out voltage. Since XRD does not show any evidence of crystallinity, it is evident that RTP anneals of the deposited thin film cannot produce a crystalline film nor can a heated-substrate-deposition at 200 C. Increasing the RTP anneal temperature is not possible due to delamination of the film and/or indium interlayer diffusion, and the system is physically limited to a maximum substrate deposition temperature of 200 C. The inability of the

current equipment to produce crystalline films may explain the discrepancies in the values for $E_{opt}$ measured for the different target compositions and the values reported by Kubota *et al.* [19]. To further develop an efficient ACTFEL phosphor, the ability to deposit thin-films at temperatures from 400 C to 500 C is required. Until our sputtering system is modified to achieve this or a new system is constructed, no further development of ACTFEL phosphors using an AlInON film sputtered from a $Al_{0.9}In_{0.1}$:$EuF_3$ target is possible.

In summary, no further evaluation of AlInN as ACTFEL phosphor is possible until the oxygen incorporated into the deposited thin-film can be eliminated. At that time, re-evaluation of the 20/60/0 film will determine whether a new target with a larger bandgap is required. The substrate temperature is a deposition parameter that should be evaluated further at temperatures above 200 C.

# CHAPTER 5 - CONCLUSIONS AND RECOMMENDATIONS FOR FUTURE WORK

This thesis describes the development and characterization of AlInON thin films as ACTFEL display phosphors. A better understanding of the development and evaluation process is gained, although no efficient phosphors are produced. The accomplishments made and problems identified are presented below along with recommendations for future work.

## 5.1 Conclusions

Several accomplishments are made in the ACTFEL phosphor development process. The refractive index of the deposited thin film is shown to be a useful indicator of run-to-run reproducibility and a general indication of changes in film composition. Measuring sputter deposition rates on glass substrates with step-height measurements eliminates the uncertainty that frequently arises with ellipsometry measurements of deposited thin film thicknesses over 1500 Å.

AES analysis shows that sputtered films are stoichiometrically similar to the sputter target, and AES analysis combined with electrical measurements shows that the oxygen content of sputtered films can be adjusted to produce changes in the steady state phosphor field of an ACTFEL device.

$Q_i$-$V_a$ plots are shown to be an effective method for determining $C_i$ and $C_t$ for $Q_{int}$-$F_p$ plots for the sputtered films used in this thesis. C-V plots do not provide reliable estimates for $C_i$ and $C_t$ for the films in this thesis, and some degree of confidence in the $Q_{int}$-$F_p$ plot is obtained by using capacitance values measured from a $Q_i$-$V_a$ plot.

Substrate heating has a significant effect on the optical properties of deposited thin films and the electrical properties of full ACTFEL devices.

A problem with the gas manifold in the RF sputtering system is identified. The leak cannot be fixed completely without replacing the gas manifold due to the Swagelok fittings used to make the connections. The inability of the system to produce an oxygen-free AlInN film makes evaluation of AlInN as an ACTFEL phosphor impossible.

Another problem identified is with regard to the 200 C temperature limit of the substrate heater. Temperatures above 200 C should be evaluated since 200 C did not produce a crystalline thin film.

## 5.2 Recommendations for Future Work

Three recommendations for future work are given below. First, the gas manifold in the RF sputtering system should be replaced. The number of fittings should be reduced to a minimum, and VCR-type fittings should be used instead of Swagelok fittings. This would be an ideal opportunity to replace the MFCs in the system with units that have gas flow rates more suitable to the flows required by the recipes and within the ability of the pumping package to handle. The gas bottles should also be replaced with new ones, and the new bottles analyzed for content prior to use in the system.

Second, the RF sputtering system should be reconfigured to allow higher substrate temperature depositions. The glass viewport should be replaced with a stainless steel plate or the roof of the deposition chamber should be redesigned. Redesigning the substrate holder should be considered also.

Third, terbium and thulium should be evaluated as luminescent impurites in an AlInN host lattice. Both Tb and Tm have valence and size compatibility with AlInN and could provide all the primary colors in one host lattice.

## REFERENCES


1) T. Inoguchi, M. Takeda, Y. Kakihara, Y. Nakata, M. Yoshida (1974), *Digest of the 1974 SID International Symposium*, Los Angeles, CA: Society for Information Display, pp. 84-85.

2) T. Ogura, A. Mikami, K. Tanaka, K. Tanaguchi, M. Yoshida, S. Nakajima (1986), *Appl. Phys. Lett.* **48**, pp. 1570-1571.

3) H. Ohnishi, Y. Yamasaki, R. Iwase (1986), *Proc. Soc. Inf. Disp.* **28**, pp. 345-350.

4) R.T. Tuenge, J. Kane (1991), *Digest of the 1991 SID International Symposium*, Playa del Rey, CA: Society for Information Display, p. 279.

5) T. Miyata, T. Minami, S. Takata, I. Fukuda (1991), *SID 1991 Digest*, pp. 286-289.

6) W.M. Ang (1992), M.S. Thesis, Oregon State University.

7) T. Nguyen (1993), M.S. Thesis, Oregon State University.

8) F. Kido, K. Matsuda, Y. Yoshikawa, M. Tamatani (1991), U.S. Patent #5,029,320.

9) A. Mikami, K. Terada, K. Okibayashi, K. Tanaka, M. Yoshida, S. Nakajima (1991), *J. Cryst. Growth* **110**, pp. 381-394.

10) K. Hirabayashi, H. Kozawaguchi, B. Tsujiyama (1987), *Jpn. J. Appl. Phys.* **26**, pp. 1472-1476.

11) S.M. Sze, ed., VLSI Technology, 2nd edition, McGraw-Hill, 1988.

12) A.A. Douglas (1993), M.S. Thesis, Oregon State University.

13) A.A. Douglas, J.F. Wager (1992), SID 1992 Digest, p. 356.

14) E. Bringuier (1989), *J. Appl. Phys.* **66**, pp. 1314-1325.

15) G.O. Mueller, R. Mach, B. Selle, G. Shulz (1988), *Phys. Stat. Sol.* (A) **110**, p. 657.

16) A. Abu-Dayah, S. Kobayashi, J.F. Wager (1993),
*Appl. Phys. Lett.* **62** (7), pp. 744-746.

17) J.D. Davidson, J.F. Wager, R.I Khormaei, C.N. King, R. Williams (1992),
*IEEE Transactions on Electron Devices* **39** (5), pp. 1122-1128.

18) A. Abu-Dayah (1993), M.S. Thesis, Oregon State University.

19) K. Kubota, Y. Kobayashi, K. Fujimoto (1989),
*J. Appl. Phys.* **66** (7), pp. 2984 - 2988.

20) Landolt-Börnstein, New Series, **17a**, Springer-Verlag, 1987.